UNIVERSITY OF CALIFORNIA,
IRVINE

Detection and Characterization of Anharmonic Overtone Vibrations of Single Molecules using Inelastic Electron Tunneling Spectroscopy

THESIS

submitted in partial satisfaction of the requirements
for the degree of

MASTER OF SCIENCE

in Physics

by

Gregory Allen Czap

Thesis Committee:
Professor Wilson Ho, Chair
Professor Ruqian Wu
Professor Ilya Krivorotov

2018

DEDICATION

To Susan, my parents, step-parents, parent-in-laws, and siblings.

They say it takes a village to raise a child, and my village is large and filled with love.

TABLE OF CONTENTS

LIST OF FIGURES

LIST OF TABLES

ACKNOWLEDGMENTS

I must thank first and foremost my Advisor Prof. Wilson Ho, who encouraged, supported and mentored me throughout this work, from conception to execution. I would also like to thank my partners Dr. Zhumin Han and Peter Wagner who worked with me to design the experiment, acquire the data and compose the scientific story.

I am grateful also to my Master's Thesis committee members Prof. Ruqian Wu and Prof. Ilya Krivorotov, along with my Ph.D. committee members Prof. Kumar Wickramasinghe and Prof. Zuzanna Siwy.

I would like to also extend my sincere gratitude to other members of the Ho group who have mentored, assisted and commiserated with me throughout the years. The other former members of the mK-STM team, Dr. Chi-Lun Jiang and Dr. Chen Xu, had a major impact on my development as an experimentalist along with Dr. Zhumin Han. Dr. Shaowei Li and Dr. Calvin J. Patel were also mentors with whom I shared a great deal of camaraderie. Along with Dr. Han, they journeyed with me to New Orleans to present this work at APS March Meeting 2017, which ended up being one of the most enjoyable and enlightening experiences of my adult life. Current members Peter Wagner, Christian Kim, Likun Wang, Jiang Yao, Siyu Chen and Yunpeng Xia, and former members Dr. Freddy Toledo, Dr. Han Kyu Lee, Dr. Haigang Zhang, Dr. Hikari Kimura, Dr. Wei Tao, Dr. Ungdon Ham and Prof. Xi Chen also have my gratitude.

I cannot emphasize enough that without the love, support and financial assistance from my family members, none of this would have been possible for me to accomplish.

Finally I would like to thank the sources of funding which made my research possible:

The Condensed Matter Physics Program, Division of Materials Research, National Science Foundation Grant No. DMR1411338.

The Chemical Sciences, Geosciences, and Biosciences Division, Office of Science U.S. Department of Energy Grant No. DE-FG02-04ER15595 and DE-FG02-06ER15826.

The Office of Naval Research Grant No. N00014-16-1-3150.

ABSTRACT OF THE THESIS

Detection and Characterization of Anharmonic Overtone Vibrations of Single Molecules using Inelastic Electron Tunneling Spectroscopy

By

Gregory Allen Czap

Master of Science in Physics

University of California, Irvine, 2018

Professor Wilson Ho, Chair

Inelastic Electron Tunneling Spectroscopy with the Scanning Tunneling Microscope (STM-IETS) is a powerful technique used to characterize vibration and spin at the single molecule level. While IETS lacks hard selection rules, historically it has been assumed that vibrational overtones are rarely seen or even absent. Here we provide direct experimental evidence that the hindered rotation overtone excitation of CO molecules on Ag(110) can be detected with STM-IETS by isotope substitution. We also show that the anharmonicity of the overtone excitation can be characterized and compared between unique adsorption sites, and find evidence of anisotropy in the vibrational anharmonicity for CO adsorbed on the $[1\bar{1}0]$ step edge.

CHAPTER 1

Introduction and Experiment Background

1.1 A Brief Review of Molecular Vibrations and Spectroscopy

Vibrational spectroscopy is among the most important tools for identifying chemical compounds. In a single molecule of a substance, the chemical bonds that glue the atoms of the molecule together are not perfectly rigid, allowing the atoms to be stretched, compressed and bent relative to one another as if they were spheres connected by stiff springs. The masses of the spheres (atoms) are determined by their element and isotope, while the stiffness of the springs (bonds) connecting them is determined by the nature of the chemical bond holding the atoms together. Since the masses are element-specific and the spring stiffness is context-specific, the resonance frequency of this mass-spring system is highly sensitive to the chemical identity that is vibrating. The carbon-carbon bonded pair, for example, has a markedly different vibrational frequency (1600-1800 cm^{-1}) than a carbon-hydrogen bonded pair (3100-3500 cm^{-1}) [1]. This sensitivity allows specific element-bond combinations to be identified directly through measurements of their vibration frequencies, providing an essential fingerprint that can reveal the identity of an unknown chemical species.

There are many different tools one can use to probe the vibrational frequencies of a compound, and by far the most common are light-based methods. However, spectroscopies based on scattering of massive particles exist which use electrons, neutrons [2] or even helium atoms [3]. In all cases, probe particles are sent into a material, and if the probe particles interact with the atoms or molecules in the material, they may lose energy to vibrations (by being

scattered or absorbed), and then one attempts to detect that this energy has been lost. By measuring this energy loss as a function of the incoming probe energy (typically by tuning the wavelength of light or the kinetic energy of the massive particles), it is straightforward to resolve absorption/scattering due to vibrations with frequencies that correspond to the energy lost.

To a first approximation, one can describe the stretching and compressing behaviors of chemical bonds in a very similar way one would describe a mechanical (and classical) spring system, albeit within the framework of quantum mechanics. This is known as the quantum harmonic oscillator model, with Hamiltonian:

$$\widehat{H} = \frac{\hat{p}^2}{2m} + \frac{1}{2}k\hat{x}^2,$$

The coefficient k serves the same role as the spring constant of a classical spring.

Obtaining the eigenvalues and eigenvectors for this system is a textbook problem in introductory quantum mechanics coursework [4], and using the above Hamiltonian in the time-independent Schrödinger equation one finds the solutions:

$$E(n) = \hbar\omega\left(n + \frac{1}{2}\right), \quad n = 0, 1, 2, 3 \ldots$$

and

$$\omega = \sqrt{\frac{k}{\mu}}$$

Here ω is a characteristic resonance frequency, k is the spring constant of the bond and μ is the effective mass of the oscillating system. The states are seen to form a "ladder", with the bottom rung "ground state" having energy $E(0) = \frac{1}{2}\hbar\omega$ and subsequent states $n > 0$ climbing increasingly high in energy in increments of $\hbar\omega$ as depicted in Fig. 1.1.

In real chemical bonds, the stiffness of the bond is not exactly like a real spring, only approximately. Whereas a spring will behave harmonically so that the restoring force increases linearly with the distance stretched or compressed, chemical bonds exhibit varying degrees of anharmonicity. For the most part, real bonds become increasingly stiff as they are compressed and increasingly soft as they are pulled apart, until the bond breaks. Although the quantum harmonic oscillator model is used as a first approximation to describe chemical bonds as they vibrate, it is a poor approximation when the atoms are located far away from equilibrium. The canonical model used to more accurately describe real chemical bonds is the Morse oscillator, with its corresponding Morse Hamiltonian of the form:

$$\widehat{H} = \frac{\hat{p}^2}{2m} + D_e\,(1 - e^{-a(\hat{x}-r_e)})^2$$

$$a = \sqrt{\frac{k}{2\,D_e}}$$

Here D_e is a new quantity that represents the energy required to break the chemical bond. This Hamiltonian also yields exact solutions from the time-independent Schrodinger equation, with eigenvalues:

$$E(n) = \hbar\omega\left(n + \tfrac{1}{2}\right) - \chi_e\hbar\omega\left(n + \tfrac{1}{2}\right)^2, \quad n = 0, 1, 2, 3 \ldots$$

$$\chi_e = \frac{\hbar\omega}{4\,D_e}$$

Example harmonic and anharmonic (Morse) potential energy curves are shown in Fig. 1.2. On inspection it is reasonable that the Morse potential should give a better description of real bonds since it accounts for the breaking of the bond as the two atoms are pulled apart. Note the similarity of the above Morse potential energy levels to the Harmonic potential case, except that there is a new additional term that represents the anharmonicity of the bond. The coefficient χ_e is

known as the anharmonicity constant and has a typical value of order 0.01 [1]. For highly vibrationally excited atoms in which $n \gg 1$, even the Morse potential begins to fail to describe real bonds and additional corrections must be used for the energy eigenvalues, necessitating additional anharmonicity coefficients beyond χ_e [5]. In general the larger these coefficients, the more anharmonic the bond is and accordingly anharmonic effects will play a more important role in the physical system under study. For most systems however, the first several vibrational states are well enough described by the Morse potential that useful information can be extracted from experimentally derived estimates of χ_e, as will be discussed in the next section.

Among the variety of spectroscopy techniques available to an experimentalist, each has advantages and disadvantages in different situations, but an important feature of vibrational spectroscopy techniques in general is that many obey selection rules. This means that for a given technique only certain kinds of vibrations can actually be detected, with the rules usually based on some kind of symmetry. For example, infrared absorption spectroscopy obeys the dipole selection rule, which states that only vibrations of atoms which result in a dynamically oscillating charge dipole when excited are infrared-active. In contrast, for Raman spectroscopy (in which light inelastically scatters off of a molecule rather than being totally absorbed), only vibrations that result in an oscillating polarizability can be observed. This selection rule is modified for molecules on metal surfaces so that only vibrations which involve an oscillating charge dipole perpendicular to the surface can be readily observed [6]. It is often critical that an experimentalist understands the selection rules of the technique being used, since the absence of a vibration in a certain frequency range can sometimes convey as much information as the presence of vibrations. A full “fingerprint” then constitutes both the observed and unobserved

vibrational states in a compound, and using multiple vibrational spectroscopy techniques with different selection rules can give complimentary information.

The anharmonicity of real chemical bonds may seem like a small detail, but it can have important implications for the proper identification of chemical compounds, their adsorption geometries on surfaces, and the binding (dissociation) energy holding atoms together or to a surface. This is particularly true for vibrational excitations beyond the first harmonic excitation, so-called overtones, and the detection of hindered-rotation overtone modes for carbon monoxide molecules adsorbed on the Ag(110) surface is the central experimental result of this work.

1.2 Overtone Vibrations

While the deviation from harmonic spring behavior is small for the first vibrational excitation (fundamental) of a chemical bond, this deviation becomes increasingly large as the bond is excited to higher vibrational states (overtones). Since the anharmonic term in the expression for the Morse oscillator energy eigenvalues is proportional to $\left(n+\frac{1}{2}\right)^2$, overtones ($\nu(n=0) \rightarrow \nu(n \geq 2)$) are much more anharmonic compared to the fundamental ($\nu(n=0) \rightarrow \nu(n=1)$). The anharmonicity can serve as an additional fingerprint to help discriminate between chemical bonds with very similar fundamental vibrational frequencies, and provides direct information about the bond dissociation energy [7,8]. For example, one can approximate the bond dissociation energy by using measurements of the fundamental and overtones (ideally as many as can be observed) using the Birge-Sponer relationship. If only the fundamental and first overtone vibrations can be measured, this can be approximated as [9]:

$$D_0 = \frac{(3\,\nu^{(1)} - \nu^{(2)})^2}{(4\,\nu^{(1)} - 2\nu^{(2)})} - \frac{5}{4}\nu^{(1)} + \frac{3}{8}\nu^{(1)}$$

Here $\nu^{(1)} = (\nu(n=0) \rightarrow \nu(n=1))$ and $\nu^{(2)} = (\nu(n=0) \rightarrow \nu(n=2))$.

Large anharmonicity in a chemical bond leads to other important physical consequences. It turns out that light-induced overtone transitions would actually be selection rule forbidden if vibrations were perfectly harmonic [1,5]. Anharmonicity lifts the selection rule, allowing the observation of overtones in the first place. Since the anharmonicity is typically a small effect, the light absorption/scattering cross-sections (excitation probabilities) for overtones are typically an order of magnitude less than the fundamental, and decreases further by an additional order of magnitude each time one climbs the vibrational ladder to higher overtone states. While this can make it difficult to actually detect overtones, many of the most important applications of overtone spectroscopy take advantage of this fact. Since the probability to excite overtones is low, light will penetrate deeply (or completely) through many types of matter without being completely absorbed, allowing non-invasive, inexpensive spectroscopic measurements of solid objects. This is especially true for overtones of stretch modes (usually the highest frequency vibration modes of molecules), which absorb light in the so-called Near-Infrared (NIR) (780 nm – 2500 nm/4000 cm^{-1} – 12800 cm^{-1}) region of the electromagnetic spectrum. Practical applications of NIR spectroscopy are numerous, including medical imaging [10], characterization of pharmaceuticals [11], assessment of food quality in the agricultural industry [12,13], and more [14–16].

The study of overtones for molecules adsorbed on surfaces is motivated by the fact that catalytically important reactions often involve small molecules on surfaces, and that a complete understanding of these adsorbates is aided by the kind of information that overtones can provide. On the other hand, vibrational spectroscopy of molecules on surfaces can be challenging since

signals are relatively weak, especially at low coverages. The difficulty is raised further when single crystals are used in place of high surface area powders, which provides the benefit of a well defined adsorption environment at the cost of a significant reduction in the number of adsorbed molecules due to the loss of surface area [7]. Combined with the comparatively weaker overtone signal strength compared to fundamental vibrations, it should come as no surprise that only a handful of infrared absorption spectroscopy measurements of overtones on single-crystal surfaces existed by the mid 1990s [7,17–20]. Aside from light-based methods, electron-scattering methods such as electron energy-loss spectroscopy (EELS) have been used to observe adsorbate overtones in a number of systems [21–25]. However, while EELS may hold an edge over light-based methods in sensitivity, the energy resolution can be limited in comparison [26].

Considering the additional information granted by overtone vibrations and combination bands, it is clear that in the ideal case, one would be able to spectroscopically study a molecule adsorbed on a surface and obtain all of the information available from vibrational excitations, such as the vibrational frequencies of all possible modes, the anharmonicities of their overtone excitations, and the degree of coupling between different vibrational modes. This may permit exact chemical identification, knowledge of the adsorption well depth (binding energy), the diffusion barrier for lateral motion on the surface, and the degree to which the intramolecular or even intermolecular bonds of the adsorbate have been strengthened or weakened due to the binding with the substrate.

1.3 Experimental Background

All of the previously mentioned spectroscopy techniques are strictly ensemble measurements; that is, they involve measuring vibration-induced losses over an entire surface or sample. Small but important details, such as variations of binding energy, diffusion barrier or reactivity among different adsorption sites on a surface are averaged out since entire surface is being probed simultaneously. It would be preferable to be able to obtain spectroscopic measurements of just one molecule at a time, ideally combined with knowledge of its specific location on a surface and local environment. In this regard, inelastic electron tunneling spectroscopy (IETS) using the scanning tunneling microscope (STM) stands apart as uniquely suited to this task [27,28].

In an STM, an atomically sharp metal tip is brought close to an electrically conducting or semiconducting surface and a bias voltage is applied between the tip and the substrate. When the tip is approached close enough that the distance between the terminating atoms of the tip and the surface atoms is within a nanometer or less, electrons can tunnel from the tip to the sample (or vice versa if one changes the polarity of the bias voltage). This tunneling can be measured as a very small current, typically on the order of 10^{-9} Amperes, and the magnitude of the current varies exponentially with the tip-surface separation. By using an electronic feedback loop to control the tip-sample separation in order to maintain constant tunneling current, the tip height above the surface will carefully follow nanometer scale contours, and by raster scanning the tip to form a 2D image, it is possible to perform microscopy at the sub-nanometer scale. Due to this exponential dependence, the STM is very sensitive to even atomic-scale features, readily

permitting the imaging of single atoms, molecules, surfaces layers and more. A schematic diagram and scale drawings of the STM used in this work are shown in Fig. 1.3.

When an STM tip is placed directly over an adsorbed molecule, some of the tunneling current will flow through or scatter off of the molecule in the junction. If the energy of a tunneling electron, controlled by the tip-sample bias voltage, is high enough to meet or exceed the excitation energy of a vibration $\hbar\omega$, then it becomes possible for the tunneling electrons to inelastically lose some energy by exciting molecular vibrations as they tunnel. This inelastic tunneling constitutes a separate tunneling channel and adds to the normal elastic channel so that the overall conductance increases as more electrons can tunnel through. In the ideal case this manifests as a stepwise increase in conductance $\frac{dI}{dV}$, or equivalently a peak in $\frac{d^2I}{dV^2}$. In practice better signal-to-noise is obtained by directly measuring $\frac{d^2I}{dV^2}$ from the lock-in amplifier rather than obtaining $\frac{dI}{dV}$ and numerically differentiating to then obtain $\frac{d^2I}{dV^2}$. A schematic diagram of the inelastic tunneling process is shown in Fig. 1.4(a) along with example I, $\frac{dI}{dV}$ and $\frac{d^2I}{dV^2}$ measurements in Fig. 1.4(b).

It is important to note that in IETS, energy resolution is severely limited by temperature so that it is standard to perform IETS measurements at liquid helium temperatures or colder. The overall broadening of a spectroscopic feature (such as peak) is approximately given by the root mean square of three contributions [28]:

$$W_{Total} = \sqrt{{W_{Int}}^2 + {W_T}^2 + {W_{Mod}}^2}$$

W_{Int} is the intrinsic broadening of the measured peak, W_T is the temperature broadening caused by temperature-induced widening of the Fermi level of the electrodes, W_{Mod} is the modulation broadening caused by application of the lock-in bias modulation V_{rms} required for

the measurement, and W_{Total} is the final experimentally measured peak width after all sources of broadening are taken into account. This can be further simplified to the expression:

$$W_{Total} = \sqrt{{W_{Int}}^2 + (5.4\, K_B T/e)^2 + (1.7\, V_{rms})^2}\,,$$

Where K_B is the Boltzmann constant, T is the temperature, e is the elementary unit of charge and V_{rms} is the root-mean-square amplitude of the modulation applied to the bias via the lock-in amplifier.

Since most vibration fundamental modes occur in the 10 meV – 400 meV (~ 80 cm^{-1} – 3200 cm^{-1}) range, and temperature broadening alone contributes ~ 4.65 meV broadening at T = 10 K, it is clear that low temperatures are critical to obtain useful spectral resolution. At liquid nitrogen temperatures (T = 80 K) the broadening is ~ 37 meV, which severely limits the ability to discern any spectral features, hence liquid helium temperatures are typically assumed to be required for IETS measurements. On the other hand very low energy surface vibrations of adsorbates, especially physisorbed species, occur in the 0 – 50 meV window. In addition, electron spin transitions which can also be excited with IETS may require electron energies less than 1 meV. The ~ 4.65 meV broadening therefore prevents detailed study of these kinds of very low energy transitions, but the temperature can be reduced further. This can be achieved by more elaborate apparatus designs that cryopump on the rare isotope ^{3}He in a closed cycle system, resulting in sub-kelvin temperatures. At T = 600 mK the thermal broadening is reduced to just 0.275 meV permitting measurements of very soft vibrations, low energy electron spin transitions, and improved energy resolution (as low as 1 meV/8 cm^{-1}). All of the experiments shown in this work were performed with such a subkelvin STM using a closed-cycle ^{3}He refrigerator system. The resolution of very subtle isotope shifts and peak splittings in the IETS spectra shown in this work would be impossible without subkelvin temperatures.

While it is clearly advantageous to be able to acquire nano-scale topographic images of single molecules as well as their individual vibrational spectra, STM-IETS does have a central drawback. Unlike light-based spectroscopy, IETS lacks “hard” (rigidly enforced) selection rules to guide the understanding of the experimentalist. Instead, so called “propensity rules” act as soft selection rules [29–33]. There is still significant theoretical and experimental effort in trying to understand STM-IETS propensity rules [34–37], although it is noteworthy that almost all theoretical effort to this end has been directed at fundamental vibration excitations, with only recent attention focused on overtones [38].

1.4 Motivation for the CO Isotope Experiment

Historically in IETS measurements reported in the literature, overtones were infrequently observed and peaks assigned as overtones were typically extremely weak [39]. Nevertheless, it is occasionally the case that certain spectroscopic features have been assigned to overtones, lacking other obvious possibilities, but these assignments have been made in error before [40,41]. Some difficulty arises from the fact that conventional IETS measurements are ensemble measurements, preventing a clear understanding of how the details of a molecule’s adsorption site and surrounding environment affects IETS cross sections for overtones and also allowing for the possibility that unaccounted for adsorbates (contaminants) may be contributing to the spectrum. An approach using STM-IETS has the benefit of being a single-molecule measurement and also allows for precise knowledge of the adsorption site. In this respect it would be highly valuable to find an experimental model adsorbate/surface system in which overtones can be observed with STM-IETS, forming the foundation onto which further

theoretical and experimental study can be built. Insight into why overtones can appear in the model system and not in most others could reveal new physical understandings of electron transport through molecules as well as clues that may lead to methods of enhancing the cross section of overtone modes. Since the selection rules in IETS are complicated and remain a topic of current research, theoretical case-studies exist in which different functional groups or binding schemes of an adsorbate can be chosen to tune IETS cross sections [38,42–44]. In a similar manner, a system with known overtone signals can provide the experimental inputs to a theoretical case study in which adsorbate, adsorption geometry and/or tip and substrate material are varied in order to understand how the overtone signal strength can be tuned.

In the work that follows, we provide proof by isotope substitution that such a model system exists in the case of the hindered rotation vibration of carbon monoxide molecules adsorbed on a silver surface. Further, we take advantage of the unique capabilities of the STM to manually reposition single molecules in order to study the affect of adsorption geometry on the overtone anharmonicity.

1.5 Bibliography

[1] K. J. Laidler and J. H. Meiser, *Physical Chemistry*, 2nd ed. (Houghton Mifflin Company, 1995).

[2] B. S. Hudson, J. Phys. Chem. A **105**, 3949 (2001).

[3] F. Hofmann and J. P. Toennies, Chem. Rev. **96**, 1307 (1996).

[4] D. J. Griffiths, *Introduction to Quantum Mechanics*, 2nd ed. (Pearson Prentice Hall, 2004).

[5] R. S. Berry, S. A. Rice, and J. Ross, *Physical Chemistry*, 2nd ed. (Oxford University Press, Oxford, 2000).

[6] M. Moskovits, J. Chem. Phys. **77**, 4408 (1982).

[7] R. Zenobi, J. Xu, J. T. Yates, B. N. J. Persson, and A. I. Volokitin, Chem. Phys. Lett. **208**, 414 (1993).

[8] L. Lessinger, J. Chem. Educ. **71**, 388 (1994).

[9] S. Lehwald, H. Ibach, and H. Steininger, Surf. Sci. **117**, 342 (1982).

[10] M. Ferrari and V. Quaresima, NeuroImage **63**, 921 (2012).

[11] Y. Roggo, P. Chalus, L. Maurer, C. Lema-Martinez, A. Edmond, and N. Jent, J. Pharm. Biomed. Anal. **44**, 683 (2007).

[12] B. M. Nicolaï, K. Beullens, E. Bobelyn, A. Peirs, W. Saeys, K. I. Theron, and J. Lammertyn, Postharvest Biol. Technol. **46**, 99 (2007).

[13] N. Prieto, R. Roehe, P. Lavín, G. Batten, and S. Andrés, Meat Sci. **83**, 175 (2009).

[14] S. Luo, E. Zhang, Y. Su, T. Cheng, and C. Shi, Biomaterials **32**, 7127 (2011).

[15] S. Tsuchikawa, Appl. Spectrosc. Rev. **42**, 43 (2007).

[16] V. Bellon-Maurel, E. Fernandez-Ahumada, B. Palagos, J. M. Roger, and A. McBratney, Trends Anal. Chem. **29**, 1073 (2010).

[17] Y. J. Chabal, Phys. Rev. Lett. **55**, 845 (1985).

[18] P. Uvdal, M. K. Weldon, and C. M. Friend, Phys. Rev. B **50**, 12258 (1994).

[19] P. Jakob, Phys. Rev. Lett. **77**, 4229 (1996).

[20] P. Jakob and B. N. J. Persson, J. Chem. Phys. **109**, 8641 (1998).

[21] L. J. Richter, T. A. Germer, J. P. Sethna, and W. Ho, Phys. Rev. B **38**, 10403 (1988).

[22] H. Ibach, J. Vac. Sci. Technol. **20**, 574 (1982).

[23] F. M. Hoffmann and R. A. de Paola, Phys. Rev. Lett. **52**, 1697 (1984).

[24] P. Avouris and J. E. Demuth, J. Chem. Phys. **75**, 5953 (1981).

[25] D. Schmeisser, J. E. Demuth, and P. Avouris, Phys. Rev. B **26**, 4857 (1982).

[26] G. A. Somorjai, *Introduction to Surface Chemistry and Catalysis* (Wiley, New York, 1994).

[27] B. C. Stipe, M. A. Rezaei, and W. Ho, Science **280**, 1732 (1998).

[28] M. A. Reed, Mater. Today **11**, 46 (2008).

[29] N. Lorente, M. Persson, L. J. Lauhon, and W. Ho, Phys. Rev. Lett. **86**, 2593 (2001).

[30] A. Troisi and M. A. Ratner, Nano Lett. **6**, 1784 (2006).

[31] M. Paulsson, T. Frederiksen, H. Ueba, N. Lorente, and M. Brandbyge, Phys. Rev. Lett. **100**, 226604 (2008).

[32] A. Garcia-Lekue, D. Sanchez-Portal, A. Arnau, and T. Frederiksen, Phys. Rev. B **83**, 155417 (2011).

[33] J. Lykkebo, A. Gagliardi, A. Pecchia, and G. C. Solomon, J. Chem. Phys. **141**, 124119 (2014).

[34] N. Pavliček, I. Swart, J. Niedenführ, G. Meyer, and J. Repp, Phys. Rev. Lett. **110**, 136101 (2013).

[35] J.-T. Lü, R. B. Christensen, G. Foti, T. Frederiksen, T. Gunst, and M. Brandbyge, Phys. Rev. B **89**, 081405 (2014).

[36] N. Okabayashi, A. Gustafsson, A. Peronio, M. Paulsson, T. Arai, and F. J. Giessibl, Phys. Rev. B **93**, 165415 (2016).

[37] S. You, J.-T. Lü, J. Guo, and Y. Jiang, Adv. Phys. X **2**, 907 (2017).

[38] J. Lykkebo, A. Gagliardi, A. Pecchia, and G. C. Solomon, ACS Nano **7**, 9183 (2013).

[39] K. W. Hipps and U. Mazur, J. Phys. Chem. **97**, 7803 (1993).

[40] S. Gauthier, S. de Cheveigné, J. Klein, and M. Belin, Phys. Rev. B **29**, 1748 (1984).

[41] J. Igalson and J. G. Adler, Phys. Rev. B **28**, 4970 (1983).

[42] S. R. Burema and M.-L. Bocquet, Nanotechnology **23**, 315702 (2012).

[43] S. R. Burema and M.-L. Bocquet, J. Phys. Chem. Lett. **3**, 3007 (2012).

[44] A. Shiotari, H. Okuyama, S. Hatta, T. Aruga, M. Alducin, and T. Frederiksen, Phys. Rev. B **94**, 075442 (2016).

Figure 1.1: The Quantum Harmonic Oscillator. The ground state $n = 0$ has nonzero energy $E_0 = \frac{1}{2}\hbar\omega$, and excited states are incrementally $\hbar\omega$ higher in energy. The single particle wavefunctions $\Psi_n(x)$ corresponding to each state are shown as solid colored lines while the probability densities $|\Psi_n(x)|^2$ are shown as filled-in curves. The wavefunctions and densities are not normalized and are instead scaled for visual clarity. On the right hand side, eigenstates of the carbon monoxide hindered translation (HT) and hindered rotation (HR) vibrations are shown for different values of n. The smaller (darker) circle inside each atom represents the motion of the nucleus. Note that the real vibration amplitudes and eigenstates for large n likely differ from what is shown in this conceptual depiction.

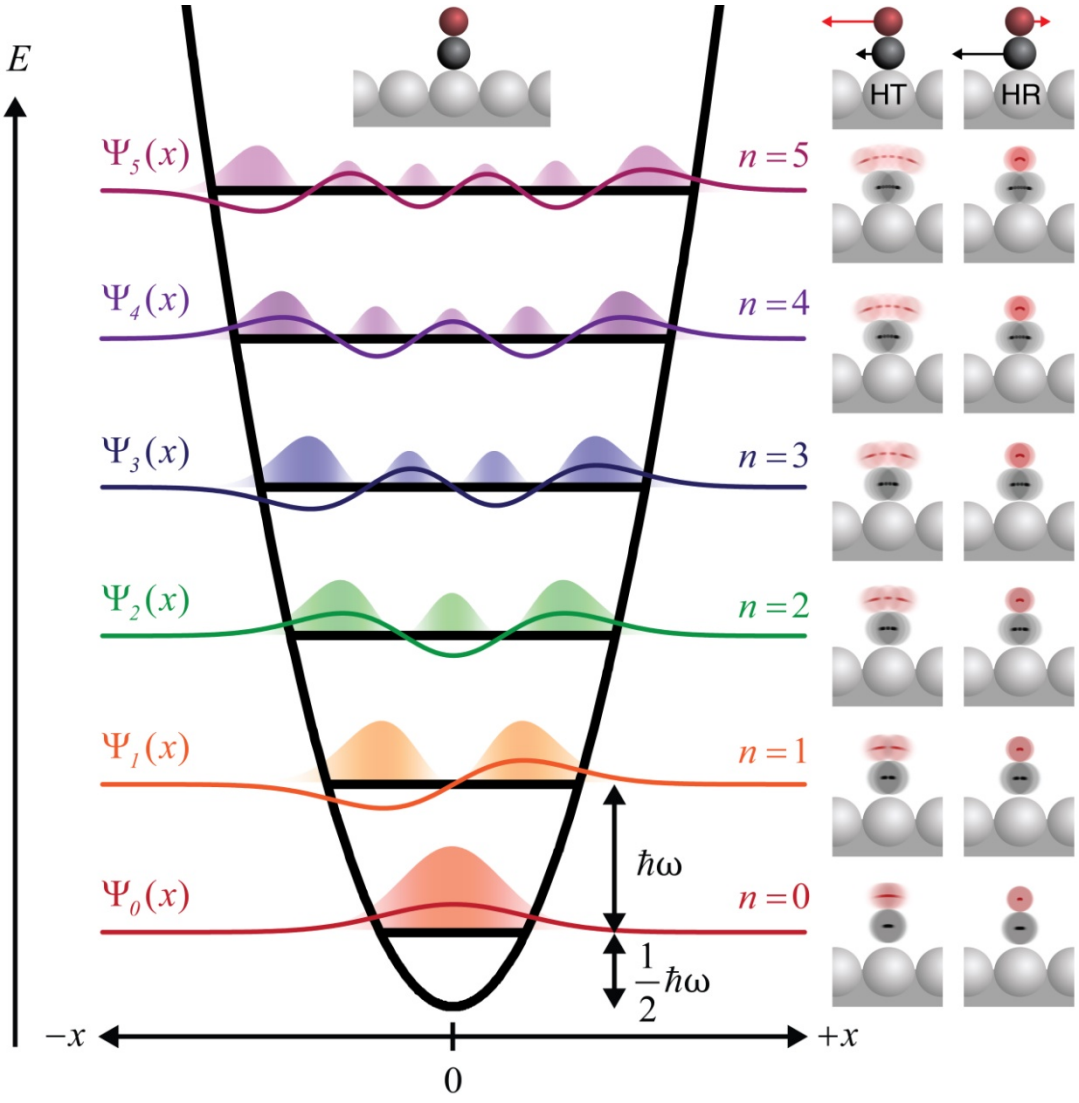
E
HT
HR
$\Psi_5(x)$
$n=5$
$\Psi_4(x)$
$n=4$
$\Psi_3(x)$
$n=3$
$\Psi_2(x)$
$n=2$
$\Psi_1(x)$
$n=1$
$\Psi_0(x)$
$n=0$
$\hbar\omega$
$\frac{1}{2}\hbar\omega$
$-x$
$+x$
0

Figure 1.2: Harmonic and Morse Potentials. The harmonic (blue) potential continues to grow unbounded as the interatomic distance $r \to \infty$, while the anharmonic Morse (red) potential levels off at D_e as $r \to \infty$, representing the breaking of the bond. Note that the real dissociation energy will be less than D_e due to the zero-point energy of the vibration so that the actual energy needed to break the bond will be $D_0 = D_e - \frac{1}{2}\hbar\omega$.

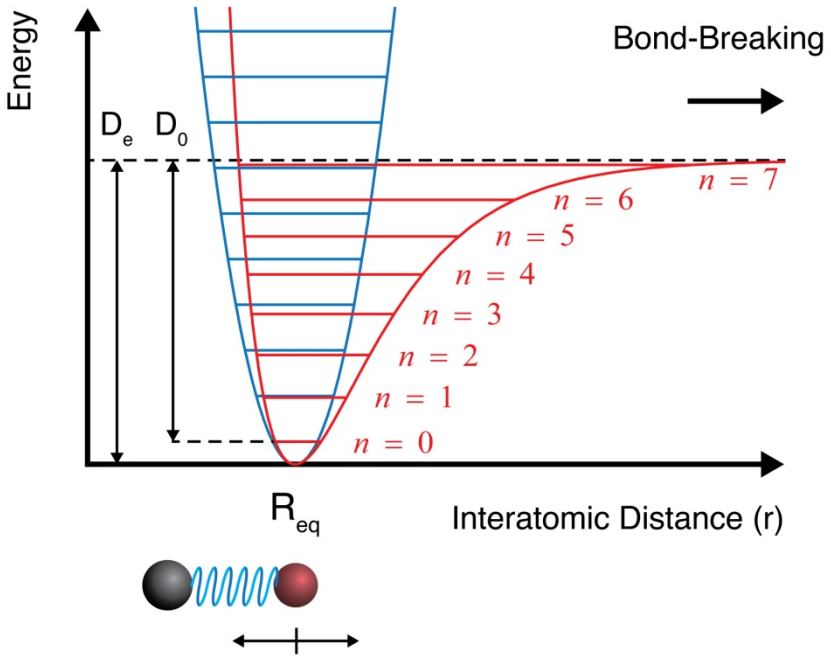
Energy
Bond-Breaking
D_e
D_0
$n = 7$
$n = 6$
$n = 5$
$n = 4$
$n = 3$
$n = 2$
$n = 1$
$n = 0$
R_{eq}
Interatomic Distance (r)

Figure 1.3: Schematic of the Ho Group STM. (a) Simplified schematic of the STM, tunneling junction and supporting electronics. (b) Scale drawing isometric view of the Ho group Besocke scanner (with sample holder lifted off the tungsten spheres for visual clarity). A tripod of piezo tubes terminating in tungsten spheres supports and translates the sample holder in the lateral (XY) plane while a fourth piezo tube located at the center of the tripod actuates the tip vertically (Z). (c) Scale drawing sample holder with silver hat-shaped sample mounted in the center. (d) Scale schematic of the scanner with a cross-section view of the sample holder. (e) Depiction of XY motion of the sample during raster scanning using the outer piezo tube tripod. (f) Depiction of Z motion of the tip using the inner tip piezo tube. Note that in (e-f) the motion of the piezo tubes is exaggerated for visibility, in reality the motions are on the scale of microns at most and are therefore not perceptible to the naked eye.

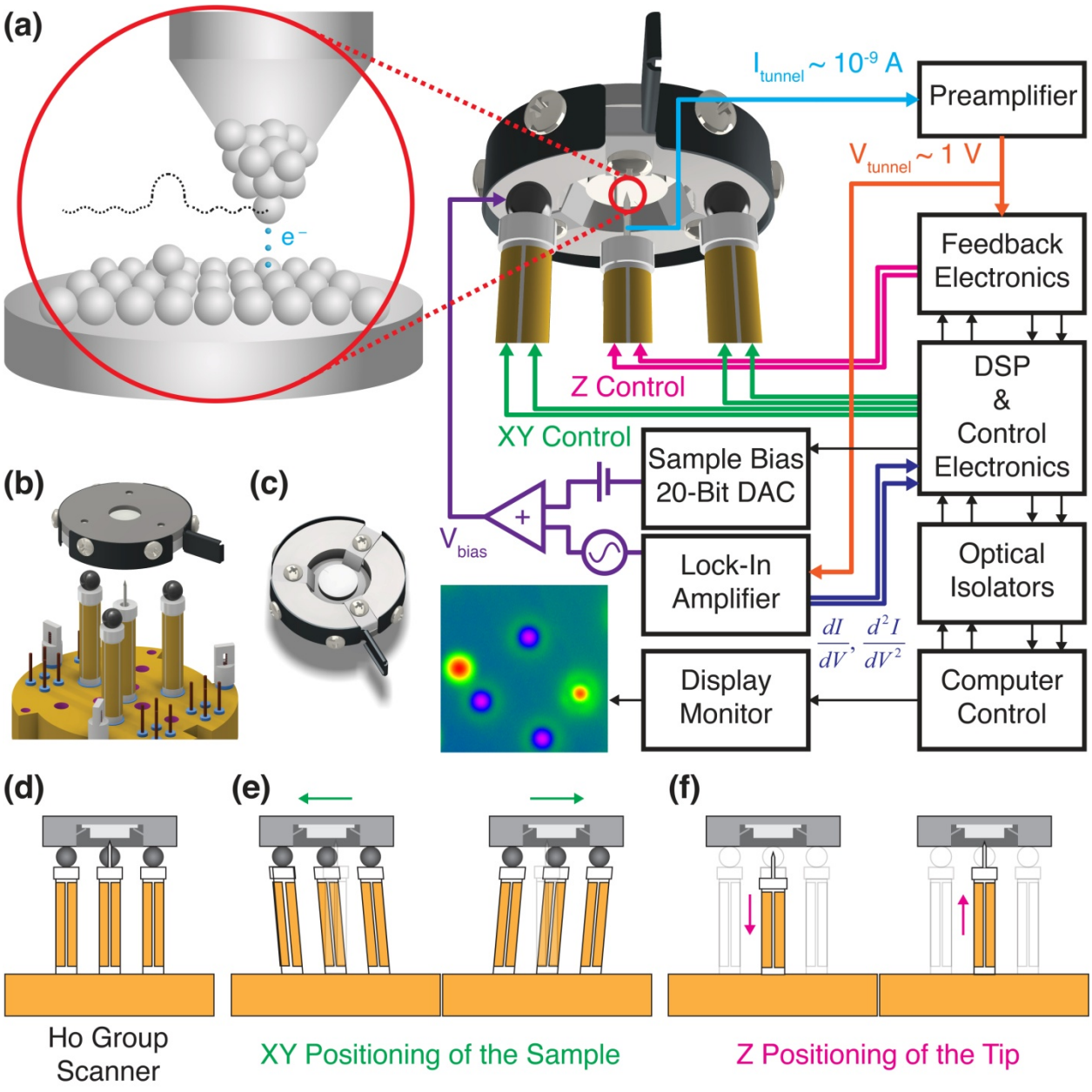
(a)
e⁻
(b)
(c)
$I_{tunnel} \sim 10^{-9}$ A
Preamplifier
$V_{tunnel} \sim 1$ V
Feedback Electronics
DSP & Control Electronics
Z Control
XY Control
Sample Bias 20-Bit DAC
V_{bias}
Lock-In Amplifier
Optical Isolators
$\frac{dI}{dV}, \frac{d^2I}{dV^2}$
Display Monitor
Computer Control
(d)
(e)
(f)
Ho Group Scanner
XY Positioning of the Sample
Z Positioning of the Tip

Figure 1.4: Schematic Diagram Depicting STM-IETS. (a) Energy level diagram for the tunneling process. With an applied bias voltage V_{bias} between the sample and tip, the Fermi level of the tip is pushed up by an amount $e \cdot V_{bias}$, allowing electrons to tunnel elastically through the vacuum gap from the tip to the sample (red arrow). If there is a molecule present in the tunneling junction, the tunneling electrons can also inelastically scatter off the molecule and lose energy to a vibration if $e \cdot V_{bias} \geq \hbar\omega$ (dark blue arrow). The resulting inelastically scattered tunneling electrons then enter the sample with energy $e \cdot V_{bias} - \hbar\omega$ (light blue dashed arrow). (b) Example STM-IETS measurements of a carbon monoxide molecule in the tunneling junction, with inelastic features corresponding to excitations of vibrational modes at ~ 2 meV and ~ 20 meV.

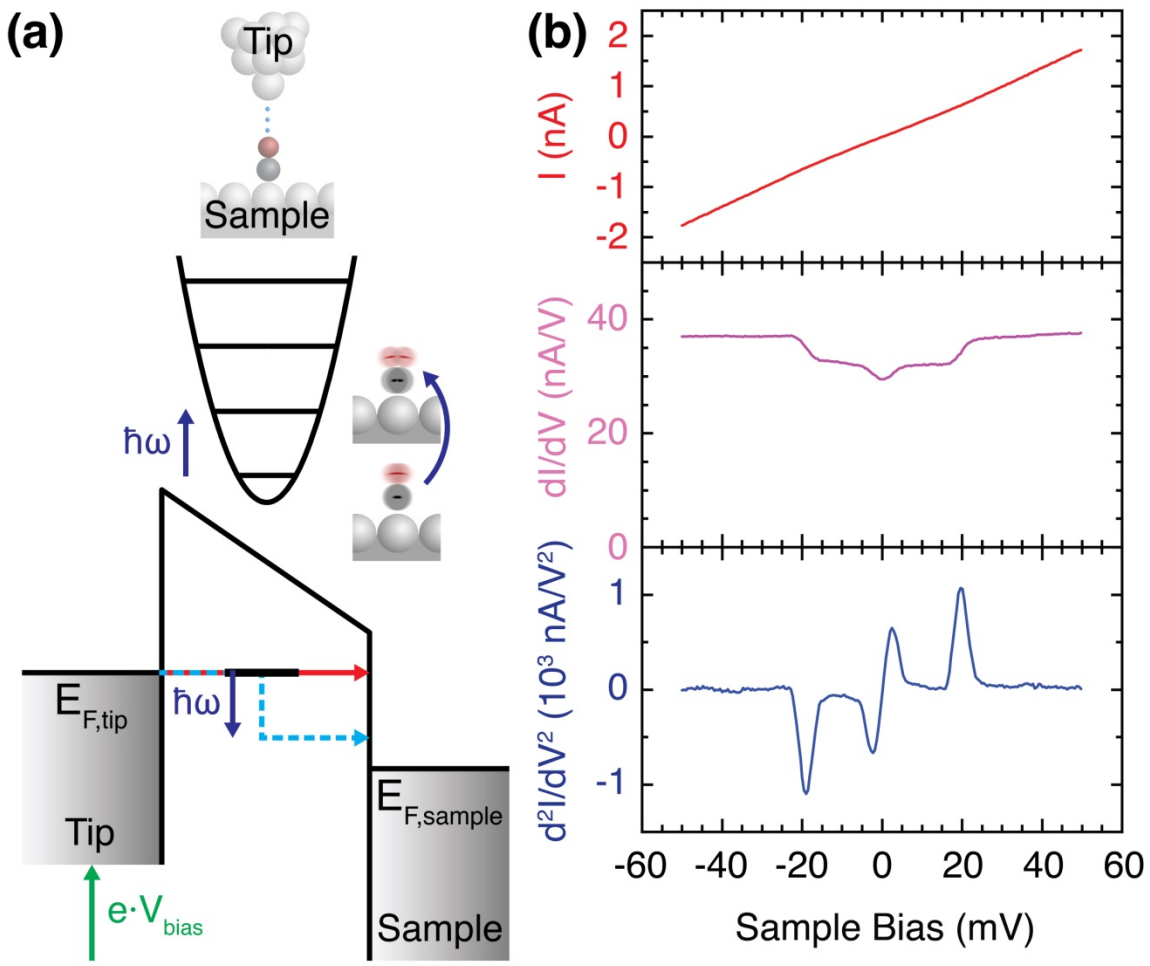
(a)
Tip
Sample
ħω
E_F,tip
ħω
E_F,sample
Tip
e·V_bias
Sample
(b)
I (nA)
2
1
0
-1
-2
dI/dV (nA/V)
40
20
0
d²I/dV² (10³ nA/V²)
1
0
-1
-60
-40
-20
0
20
40
60
Sample Bias (mV)

CHAPTER 2

Adsorption Site Specific Detection of CO Overtones with STM-IETS

2.1 Introduction and Background

Overtone vibrations of adsorbed molecules can reveal valuable information about binding energies [1–3], lateral diffusion barriers [4], and coupling between different vibrational modes [5,6] or other adsorbates [7,8]. In this context, single molecule experiments using the scanning tunneling microscope (STM) are of considerable value as they allow an unambiguous correlation between the local environment of the adsorbate and changes in its spectroscopic features, motion or reaction rates [9–11]. Overtones have been observed with the STM in the action spectra of single molecules as they diffuse or desorb [3,4], however this detection scheme requires molecules that readily undergo vibration-induced changes under the STM tip. It is highly desirable to be able to access the information contained in the overtone vibrations directly using inelastic electron tunneling spectroscopy (IETS) with the STM [12], but overtones are known to be scarcely observed in IETS [13,14].

Considerable theoretical and experimental attention has been focused on quantum interference effects in electronic transport through single molecules [15–17], which may provide routes to realizing proposed single molecule devices [18–21]. It has also been suggested that quenching the elastic transport channel in single molecule junctions by exploiting destructive quantum interference can increase the inelastic contribution to the conductance, potentially allowing observations of overtones [14]. Promising results were recently demonstrated in IETS measurements of anthraquinone molecular junctions [22], but the ensemble nature of the

measurements and the lack of isotope substitution to characterize modes assigned to overtones makes conclusive assignments challenging. At the same time carbon monoxide (CO), one of the most well studied molecules in surface science [23], is also believed to exhibit quantum interference in the STM tunneling junction [24,25]. Recently a new vibration mode of CO on Ag(110) was detected with STM-IETS [26], which was speculated to be an overtone excitation of the CO hindered rotation (HR) mode but is too energetically close to the Ag-CO bouncing mode [4] for definitive assignment.

Here we provide direct evidence that the new vibration mode detected by Han *et al.* is in fact the $\nu = 0$ to $\nu = 2$ overtone excitation of the HR mode via isotopic substitution. Further, we use STM tip manipulation to position three CO isotopes in different adsorption geometries, enabling site-specific measurements of anharmonicity and anisotropy in the vibrational potential energy surface.

2.2 Methods

Experiments were performed with a home-built subkelvin STM at a base pressure of 6×10^{-11} Torr. Chemically etched Ag tips and Ag(110) single crystal were cleaned *in situ* with several cycles of sputtering with Ne^+ followed by annealing. $^{12}C^{16}O$, $^{13}C^{16}O$, and $^{12}C^{18}O$ molecular isotopes were dosed individually through a variable leak valve onto the Ag(110) surface held at ~26 K. The sample was then cooled to 600 mK for all measurements. CO molecules were transferred to the tip by performing constant-current STM scans over the CO with feedback setpoint 1 mV/1 nA. CO molecules were non-destructively returned to the surface by ramping to the feedback setpoint 1.5 V/1 nA, waiting for a ~ 0.5 Å change in the feedback Z,

then quickly ramping the bias to < 100 mV to prevent the new surface-adsorbed CO from laterally hopping or desorbing. Unless otherwise noted all STM-IETS measurements were acquired with feedback setpoint 10 mV/300 pA.

2.3 Results and Discussion

CO molecules adsorbed on the Ag(110) surface appear as dark depressions in constant current STM topography as shown in Fig. 2.1(a). Upon transferring a CO molecule to the STM tip, the depression disappears from the surface and the topography exhibits greatly enhanced contrast, permitting resolution of the individual Ag(110) surface atoms as in Fig. 2.1(b). Intense peaks appear in d^2I/dV^2 measurements shown in Fig. 2.1(c), which correspond to the hindered translation (HT) and HR modes of CO on the surface as depicted schematically in Fig. 2.1(d). In addition, a new feature is observed at 37.1 mV (35.6 mV) for the CO adsorbed on the terrace (tip) as reported recently [26]. The identity of this new mode was speculated to be the overtone of the HR mode, however the energetic proximity to the Ag-CO bouncing mode (~ 31 meV) [4] prevents definitive identification. As there are sound theoretical reasons to believe that both the M-CO bouncing mode [27] and overtone modes [13,14,28] should be difficult or even impossible to observe in IETS, the observation of a new IETS feature alone does not provide adequate information to make an assignment in this case.

Previous studies of the hindered vibration modes of CO on metal surfaces [29,30] have indicated that the three surface modes shown in Fig. 2.1(d), which are the (HT), (HR) and (M-CO) modes, show distinct isotope shifts. Specifically, the HT mode largely consist of oxygen motion with a small amount of carbon motion, so that it is more analogous to a wagging mode

than a direct translation of the entire molecule [26,29]. This causes the HT mode to be more sensitive to an increase in the oxygen mass through isotope substitution compared to carbon. For the HR mode however, the vibration amplitude for the carbon atom is larger than for oxygen and it is therefore more sensitive to carbon atom isotope substitution. In contrast the M-CO mode is a translation of the entire molecule against the surface and has equal sensitivity to carbon or oxygen isotope labels. Further, the M-CO mode exhibits a smaller isotope shift compared to the other two modes since its vibration frequency is proportional to the inverse of the entire molecular mass rather than primarily the oxygen atom (HT) or carbon atom (HR) alone.

In light of the above considerations, we chose to perform high-resolution STM-IETS measurements of three different isotopes of CO in order to elucidate the identity of the new mode. Roughly equal quantities of $^{12}C^{16}O$, $^{13}C^{16}O$, and $^{12}C^{18}O$ were dosed onto the Ag(110) for this experiment. On the Ag(110) surface, the degeneracy of the CO HR mode is lifted and at small bias modulation (< 1 mV), two peaks can be readily distinguished [10]. High resolution STM-IETS measurements of the lower HR peak are shown in Fig. 2.2(a) permitting the distinction of three isotopes by inspection. With each isotope identified, individual CO molecules of each type were assembled together by tip manipulation in the constant current STM image in Fig. 2.2(b). High resolution IETS spectra with more passes averaged were then obtained for all three isotopes adsorbed on the terrace as shown in Fig. 2.2(c), all with the same tip apex termination. Similar to the HR mode, the HT mode degeneracy is also lifted due to the surface anisotropy. In addition, a small peak feature near zero bias appears. This has been reported before as a Zero Bias Conductance Dip and is also present with the tip positioned over the bare surface [31,32]. Isotope shifts for both vibration modes are readily apparent for the ^{13}C and ^{18}O substituted CO, with the shift in the HR mode (right panel) amounting to ~ 0.55 mV for $^{13}C^{16}O$

and ~ 0.15 mV for $^{12}C^{18}O$. Notably, the isotope shift for the HT mode (left panel) follows the opposite trend, with a barely discernible shift of ~ 0.05 mV for $^{13}C^{16}O$ and a more obvious shift of ~ 0.15 mV for $^{12}C^{18}O$. These results indicate that the red isotope (center) is $^{13}C^{16}O$ while the blue isotope (bottom) is $^{12}C^{18}O$.

Measurements of the new vibration mode for all three isotopes will yield clues needed for its identification. If the new mode is the Ag-CO bouncing mode, then the isotope shift for the $^{12}C^{18}O$ species should be largest since it has the greatest overall mass increase. However if it is an overtone of the HR mode, then the $^{13}C^{16}O$ species should exhibit a much larger isotope shift, around twice that of the HR mode. High resolution IETS measurements of the unidentified peak are shown in Fig. 2.3(a) for all three isotopes adsorbed on the terrace, without background subtraction. While the signal strength is low owing to the greatly decreased IETS cross section compared to the HR fundamental, an obvious isotope shift of ~ 0.90 mV for the $^{13}C^{16}O$ species compared to ~ 0.35 mV for $^{12}C^{18}O$ strongly suggests that the new vibration mode is the $\nu = 0$ to $\nu = 2$ HR overtone excitation. Another key finding is that the overtone exhibits an anharmonicity of ~ 1.5 % (see Supporting Materials). In addition, the overtone appears as a doublet with the higher energy peak curiously having significantly lower intensity than the lower energy peak. A schematic diagram depicting the overtone excitation for example harmonic and anharmonic potentials is shown in Fig. 2.3(b).

As the signal strength for the HR overtone is significantly stronger on the tip than on the terrace, high resolution measurements of the vibrational spectrum were repeated one at a time for each CO isotope adsorbed on the tip. The CO molecules were controllably transferred to the same metal tip apex termination and back to the surface in all cases. Plots of HR and HR overtone measurements are shown in Fig. 2.3(c). In contrast to the Ag(110) top site, the

symmetric Ag tip is a more isotropic adsorption geometry and the HR doublet remains degenerate. For this reason, the HR overtone would be expected to appear as a solitary, more intense peak. The HR mode of the CO isotopes adsorbed on the tip in Fig. 2.3(c) follow the same isotope shifts as on the terrace in Fig. 2.2(d), and the HR overtone indeed appears as a single, more intense peak which also follows the same isotope shifts, yielding a consistent anharmonicity across isotopes of 1.9 % ± 0.15%. Based on the CO isotope measurements on the terrace and on the tip, a definitive assignment of the new peak as the HR overtone can be made.

An anisotropic adsorption environment can give rise to anisotropy in a molecule's motion within that environment. This is observable as direction-dependent diffusion rates [33] or inequivalent vibrational frequencies along different lattice directions [34] as seen in this work. Another possibility is that the *anharmonicity of a molecular vibration can be anisotropic* [35]. While the Ag(110) surface has 2-fold D_{2h} symmetry which lifts the degeneracy of the HR mode and its overtone, the weak signal and close energetic proximity of the HR overtone doublet peaks for CO adsorbed on the terrace makes precise determination of peak positions challenging. To examine the overtone in a more anisotropic environment where the HR doublet will split further, we repeated the CO isotope IETS measurements for CO adsorbed on the Ag(110) $[1\bar{1}0]$ step edge. Each CO isotope was transferred from the terrace to the tip, and then from the tip to the step edge in sequence. IETS measurements of the $^{12}C^{16}O$ HR and HR overtone are shown in Fig. 2.4(a). The HR spectra (top) shows a remarkable increase in the doublet splitting from ~ 1.7 mV on the terrace to ~ 2.6 mV on the $[1\bar{1}0]$ step edge, so that the peaks are now well separated. The HR overtone peaks (bottom) are also more separated which permits improved peak fitting. To provide a direct visualization of the anharmonicity among different isotopes and adsorption environments, a plot of the lower doublet peak positions of the HR overtone vs the HR

fundamental is shown in Fig. 2.4(b). The peak positions are featured with the standard errors of their peak fits and are compared with the y = 2 x line in order to emphasize the anharmonicity in each measurement. While the CO isotopes in the terrace and step edge geometries seem to have similar anharmonicities, the tip geometry has a noticeably larger deviation from the y = 2 x line and therefore a larger anharmonicity. Constant current topography of the three CO isotopes on the step edge taken with bare Ag tip is shown inset in Fig. 2.4(b). Topography taken with a CO terminated tip at close tunneling gap yields atomic resolution of the Ag(110) surface and confirms that CO adsorbs on the atop sites of the terminating atoms of the step edge (Supplementary Materials). A plot of the higher doublet peak positions of the HR overtone vs HR fundamental is shown in Fig. 2.4(c). In this case the anharmonicity of the step edge peak seems greater than that of the terrace. A plausible physical explanation is that the anharmonicity is anisotropic, so that vibrations along the step edge are more (or less) harmonic than vibrations against (perpendicular to) the step edge. Curiously, while intuition might predict that the softer vibration direction ([001] direction) is more anharmonic, it seems that vibrations along the step edge have simultaneously blueshifted and become more anharmonic compared to CO on the terrace. This is unexpected, and we hope that these results will garner theoretical interest in accounting for this observation.

2.4 Conclusions

In summary, STM-IETS measurements of three CO isotopes in several adsorption geometries on Ag(110) conclusively demonstrate the observation of overtone vibrations with IETS and provide the first adsorption site-specific measurements of vibration anharmonicity at the single-molecule level. Our experimental results constitute a series of simple, well characterized benchmark geometries for the theoretical treatment of overtones in STM-IETS and further lends credence to recent assignments of phonon overtones in IETS measurements of 2D materials [36,37], C=C and C-H bending mode overtones in cross-conjugated molecular junctions [22] and an N-H bending overtone Fermi resonance in STM dI/dV measurements of porphycene on Cu(110) [6] .

2.5 Bibliography

[1] R. S. Berry, S. A. Rice, and J. Ross, *Physical Chemistry*, 2nd ed. (Oxford University Press, Oxford, 2000).

[2] D. Schmeisser, J. E. Demuth, and P. Avouris, Phys. Rev. B **26**, 4857 (1982).

[3] J. I. Pascual, N. Lorente, Z. Song, H. Conrad, and H.-P. Rust, Nature **423**, 525 (2003).

[4] J. Oh, H. Lim, R. Arafune, J. Jung, M. Kawai, and Y. Kim, Phys. Rev. Lett. **116**, 056101 (2016).

[5] R. Zenobi, J. Xu, J. T. Yates, B. N. J. Persson, and A. I. Volokitin, Chem. Phys. Lett. **208**, 414 (1993).

[6] S. Liu, D. Baugh, K. Motobayashi, X. Zhao, S. V. Levchenko, S. Gawinkowski, J. Waluk, L. Grill, M. Persson, and T. Kumagai, Phys. Chem. Chem. Phys. **20**, 12112 (2018).

[7] L. J. Richter, T. A. Germer, J. P. Sethna, and W. Ho, Phys. Rev. B **38**, 10403 (1988).

[8] T. Moritz and W. Widdra, Phys. Rev. Lett. **86**, 103 (2001).

[9] T. Kumagai, F. Hanke, S. Gawinkowski, J. Sharp, K. Kotsis, J. Waluk, M. Persson, and L. Grill, Nat. Chem. **6**, 41 (2014).

[10] C. Chiang, C. Xu, Z. Han, and W. Ho, Science **344**, 885 (2014).

[11] H. J. Yang, M. Trenary, M. Kawai, and Y. Kim, J. Phys. Chem. Lett. **7**, 4369 (2016).

[12] B. C. Stipe, M. A. Rezaei, and W. Ho, Science **280**, 1732 (1998).

[13] K. W. Hipps and U. Mazur, J. Phys. Chem. **97**, 7803 (1993).

[14] J. Lykkebo, A. Gagliardi, A. Pecchia, and G. C. Solomon, ACS Nano **7**, 9183 (2013).

[15] C. M. Guédon, H. Valkenier, T. Markussen, K. S. Thygesen, J. C. Hummelen, and S. J. Van Der Molen, Nat. Nanotechnol. **7**, 305 (2012).

[16] H. Vazquez, R. Skouta, S. Schneebeli, M. Kamenetska, R. Breslow, L. Venkataraman, and M. S. Hybertsen, Nat. Nanotechnol. **7**, 663 (2012).

[17] X. Liu, S. Sangtarash, D. Reber, D. Zhang, H. Sadeghi, J. Shi, Z. Y. Xiao, W. Hong, C. J. Lambert, and S. X. Liu, Angew. Chemie - Int. Ed. **56**, 173 (2017).

[18] D. M. Cardamone, C. A. Stafford, and S. Mazumdar, Nano Lett. **6**, 2422 (2006).

[19] R. Baer and D. Neuhauser, J. Am. Chem. Soc. **124**, 4200 (2002).

[20] C. J. Lambert, Chem. Soc. Rev. **44**, 875 (2015).

[21] C. Nappi, F. Romeo, L. Parlato, F. Di Capua, A. Aloisio, and E. Sarnelli, J. Phys. Chem. C (2018).

[22] C. Salhani, M. L. Della Rocca, C. Bessis, R. Bonnet, C. Barraud, P. Lafarge, A. Chevillot, P. Martin, and J.-C. Lacroix, Phys. Rev. B **95**, 165431 (2017).

[23] G. A. Somorjai, *Introduction to Surface Chemistry and Catalysis* (Wiley, New York, 1994).

[24] J. A. Nieminen, E. Niemi, and K. H. Rieder, Surf. Sci. **552**, L47 (2004).

[25] A. Gustafsson, N. Okabayashi, A. Peronio, F. J. Giessibl, and M. Paulsson, Phys. Rev. B **96**, 085415 (2017).

[26] Z. Han, G. Czap, C. Xu, C. Chiang, D. Yuan, R. Wu, and W. Ho, Phys. Rev. Lett. **118**, 036801 (2017).

[27] A. Garcia-Lekue, D. Sanchez-Portal, A. Arnau, and T. Frederiksen, Phys. Rev. B **83**, 155417 (2011).

[28] J. Kirtley and P. Soven, Phys. Rev. B **19**, 1812 (1979).

[29] A. P. Graham, F. Hofmann, J. P. Toennies, G. P. Williams, C. J. Hirschmugl, and J. Ellis, J. Chem. Phys. **108**, 7825 (1998).

[30] L. Lauhon and W. Ho, Phys. Rev. B **60**, R8525 (1999).

[31] C. Xu, C. Chiang, Z. Han, and W. Ho, Phys. Rev. Lett. **116**, 166101 (2016).

[32] C. R. Ast, B. Jäck, J. Senkpiel, M. Eltschka, M. Etzkorn, J. Ankerhold, and K. Kern, Nat. Commun. **7**, 13009 (2016).

[33] T. Komeda, Y. Kim, M. Kawai, B. N. J. Persson, and H. Ueba, Science **295**, 2055 (2002).

[34] J. Ahner, D. Mocuta, R. D. Ramsier, and J. T. Yates, Phys. Rev. Lett. **79**, 1889 (1997).

[35] J. Braun, J. Weckesser, J. Ahner, D. Mocuta, J. T. Yates, and C. Wöll, J. Chem. Phys. **108**, 5161 (1998).

[36] F. D. Natterer, Y. Zhao, J. Wyrick, Y.-H. Chan, W.-Y. Ruan, M.-Y. Chou, K. Watanabe, T. Taniguchi, N. B. Zhitenev, and J. A. Stroscio, Phys. Rev. Lett. **114**, 245502 (2015).

[37] S. Jung, M. Park, J. Park, T.-Y. Jeong, H.-J. Kim, K. Watanabe, T. Taniguchi, D. H. Ha, C. Hwang, and Y.-S. Kim, Sci. Rep. **5**, 16642 (2015).

Figure 2.1: STM Topography and IETS of CO Molecules. (a) Constant current topography of a single CO molecule with feedback setpoint 100 mV/ 0.1 nA. (b) Constant current topography of the Ag(110) surface obtained after transferring the CO molecule to the STM tip with feedback setpoint 10 mV/ 0.3 nA, image size 20 Ångströms square. (c) STM-IETS of CO adsorbed on the Ag(110) surface (top), CO adsorbed on the STM tip (middle) and the Ag(110) surface taken with bare tip as a background measurement (bottom) . Each spectra is the average of 40 passes, taken with 2 mV_{RMS} bias modulation at 471 Hz. Inset spectra were taken with finer bias step size and averaging 80 passes. (d) Schematic diagram showing the four possible vibration modes of CO on the surface. Note that HT and HR are both normally doubly degenerate, but this degeneracy can be lifted due to surface anisotropy as in the present work.

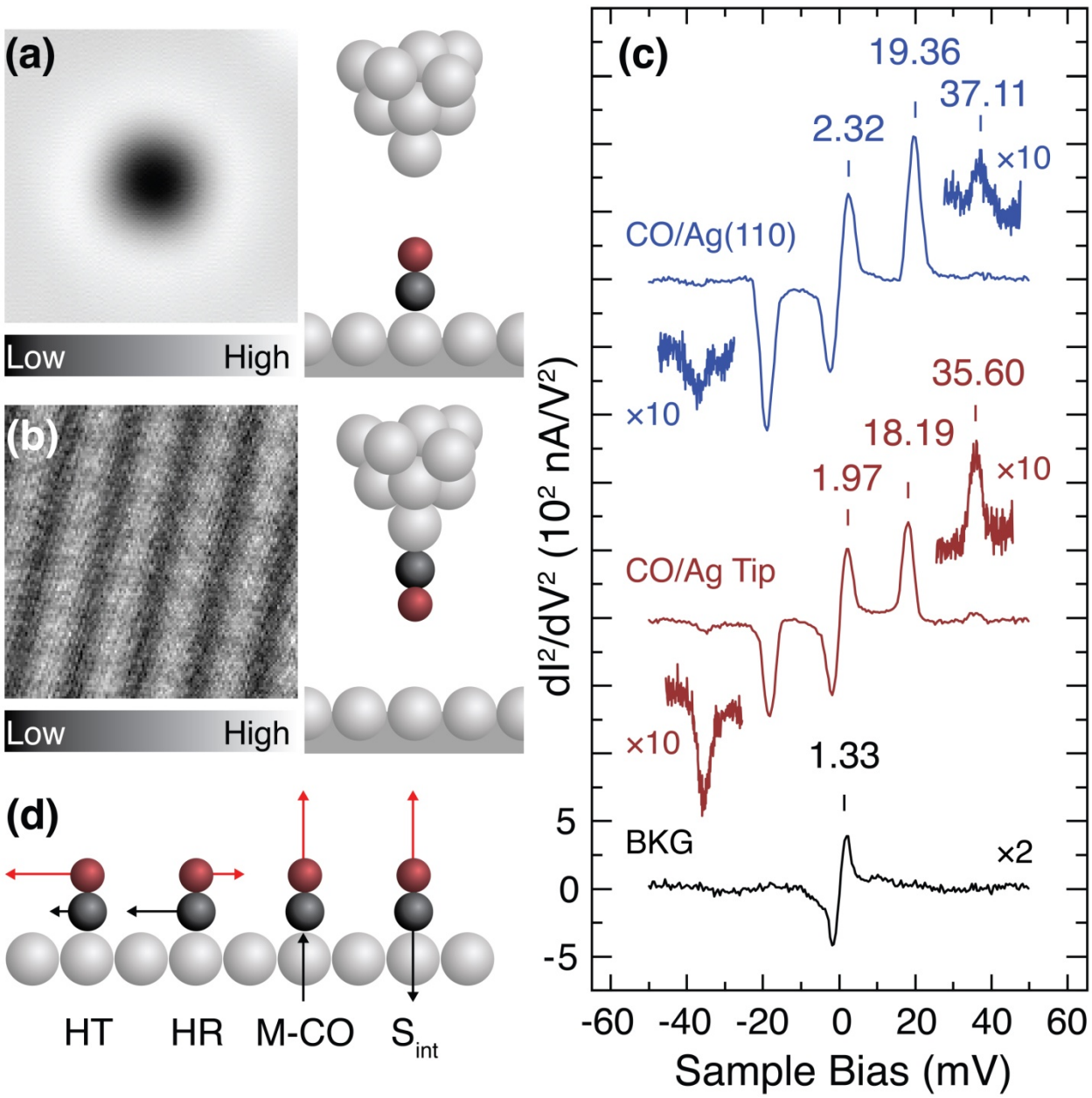
(a)
Low
High
(b)
Low
High
(c)
19.36
37.11
2.32
×10
CO/Ag(110)
×10
35.60
18.19
1.97
×10
CO/Ag Tip
×10
1.33
BKG
×2
dI²/dV² (10² nA/V²)
5
0
-5
-60
-40
-20
0
20
40
60
Sample Bias (mV)
(d)
HT
HR
M-CO
S_int

Figure 2.2: Isotope Shifts of the CO Hindered Translation and Rotation Modes. (a) High resolution plot of the HR doublet low energy peak for all three isotopes. (b) Constant current topography of three CO isotopes arranged together by tip manipulation. Isotopes were assigned by measuring IETS peak positions prior to tip manipulation and are otherwise indistinguishable in STM topography. (d) STM-IETS of the HT doublet (left panel) and HR doublet (right panel) for all three isotopes. All HT spectra were taken with 300 μV_{RMS} bias modulation at 311.11 Hz, averaged over 80 passes, while all HR spectra were taken with 600 μV_{RMS} bias modulation, averaged over 40 passes. All peak positions displayed are the average of positive and negative bias and peak position indicators for $^{12}C^{16}O$ are included for all spectra to aid comparison.

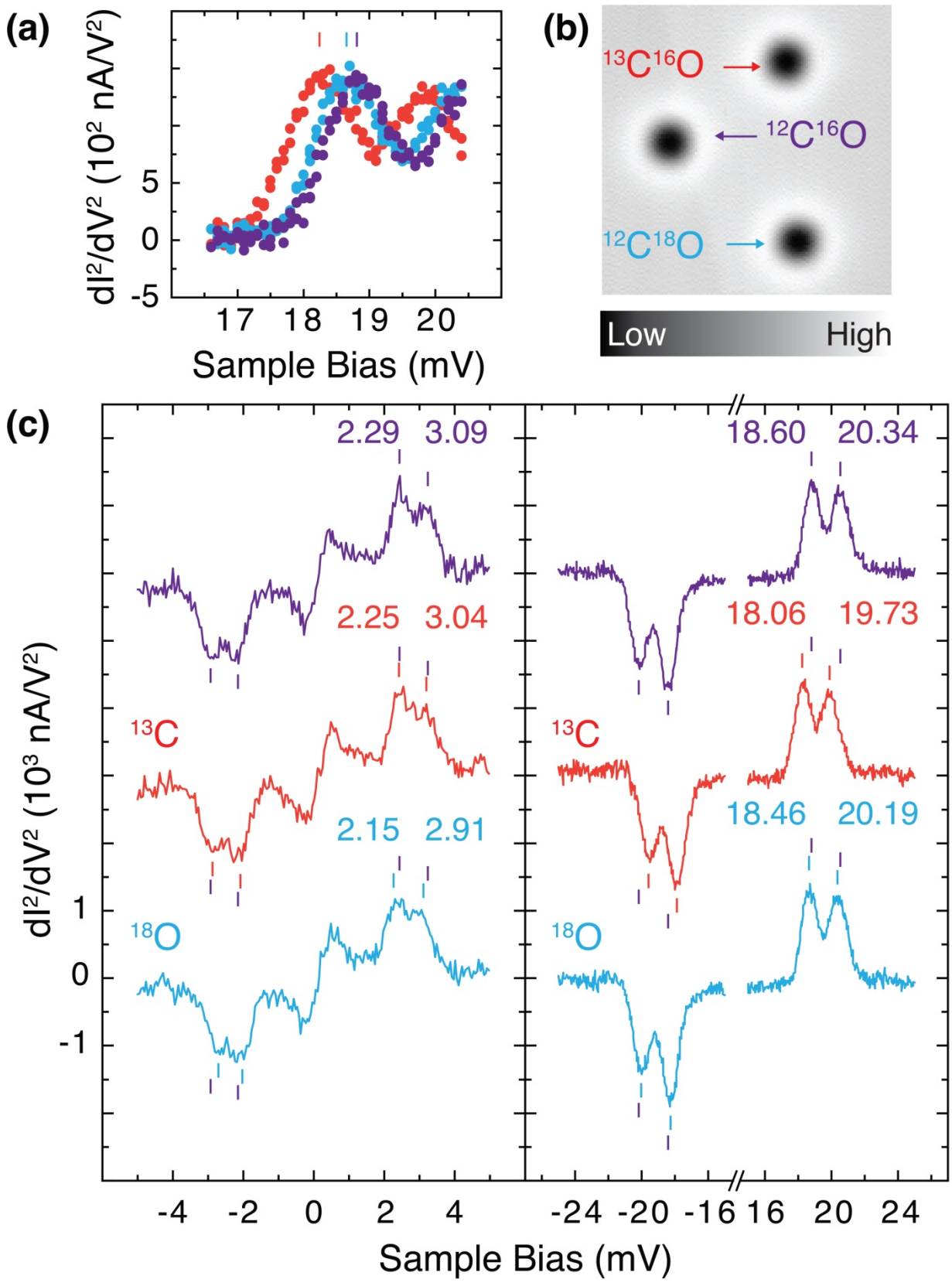
(a)
dI²/dV² (10² nA/V²)
5
0
-5
17 18 19 20
Sample Bias (mV)
(b)
13C16O
12C16O
12C18O
Low
High
(c)
2.29 3.09
2.25 3.04
2.15 2.91
18.60 20.34
18.06 19.73
18.46 20.19
13C
13C
18O
18O
dI²/dV² (10³ nA/V²)
1
0
-1
-4 -2 0 2 4
-24 -20 -16 16 20 24
Sample Bias (mV)

Figure 2.3: Isotope Shifts of the CO Hindered Rotation Mode Overtone. (a) IETS measurements of the HR overtone for all three isotopes adsorbed on the terrace taken with bare Ag tip. Each spectra was taken with 1.5 mV bias modulation at 471 Hz, averaged over 160 passes. (b) Schematic diagram illustrating the anharmonicity in vibrational energy level spacings for the HR. A harmonic potential is displayed in blue and a model anharmonic potential is displayed in red. Both potentials are functions of the vibration coordinate θ, visualized as the angle the Ag-C bond axis makes with the surface normal for conceptual simplicity. (c) STM-IETS of the HR (left panel) and HR overtone (right panel) for each CO isotope adsorbed on the tip. For all spectra in (a) and (c), peak positions are displayed as the average of positive and negative bias and peak position indicators for $^{12}C^{16}O$ are included to aid comparison.

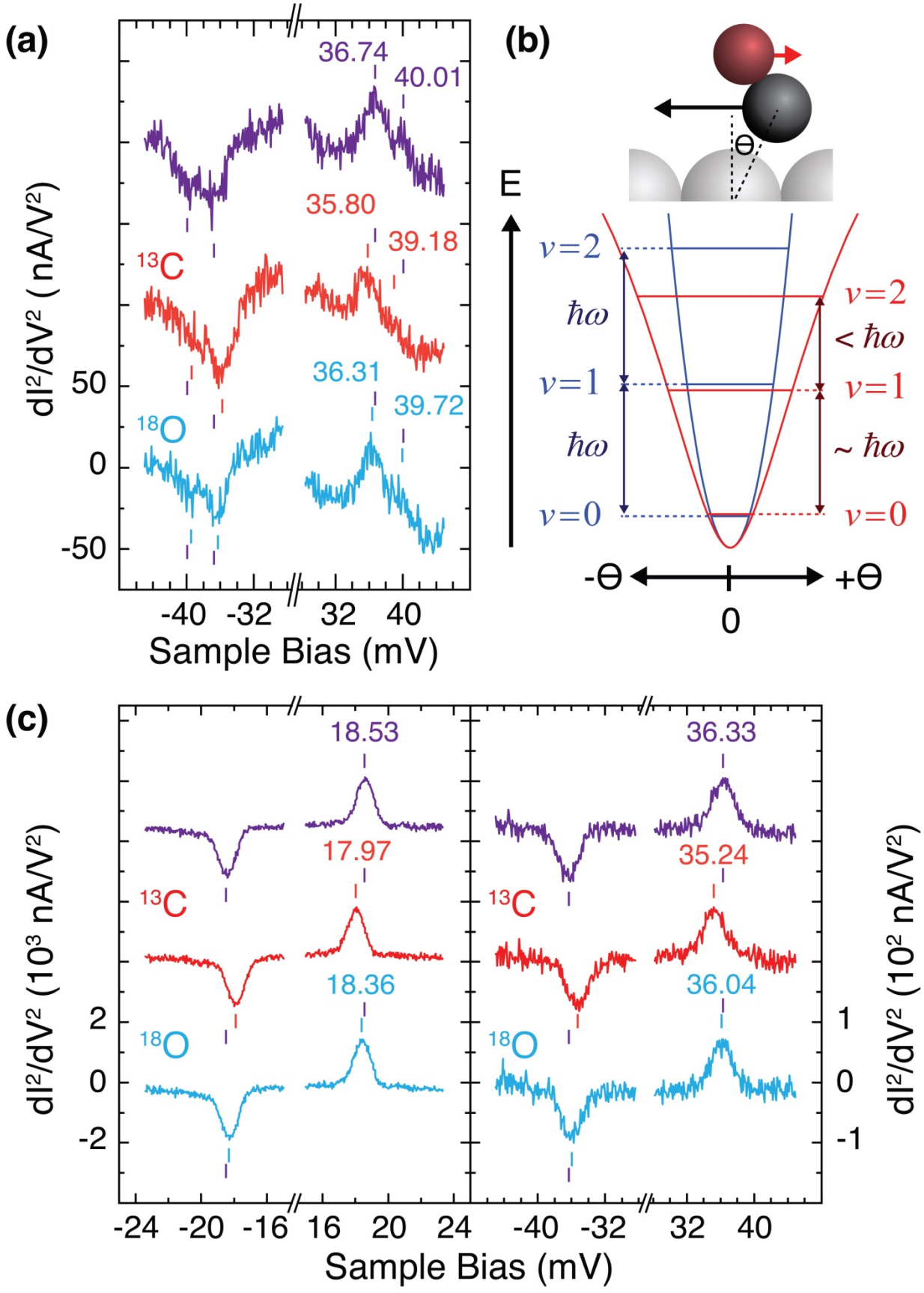
(a)
36.74
40.01
35.80
39.18
36.31
39.72
13C
18O
dI²/dV² (nA/V²)
50
0
-50
-40 -32 32 40
Sample Bias (mV)
(b)
E
Θ
v=2
ħω
v=1
ħω
v=0
v=2
< ħω
v=1
~ ħω
v=0
-Θ
+Θ
0
(c)
18.53
17.97
18.36
36.33
35.24
36.04
13C
18O
dI²/dV² (10³ nA/V²)
dI²/dV² (10² nA/V²)
2
0
-2
1
0
-1
-24 -20 -16 16 20 24 -40 -32 32 40
Sample Bias (mV)

Figure 2.4: STM-IETS of Three CO Isotopes Adsorbed on the $[1\bar{1}0]$ Step Edge. (a) STM-IETS of the HR (top) and HR overtone (bottom) for the $^{12}C^{16}O$ isotope. (b) Plot of HR overtone (HRO) vs HR low peak position for all measurements made in this work. Isotope is indicated by color and adsorption geometry by shape. Deviations from the y = 2 x line provide a visual measure of the anharmonicity in the HR overtone. (c) Plot of HR overtone vs HR high peak position. Note the absence of the tip geometry due to the degeneracy of the tip HR/HRO peaks. Inset (c) is constant current topography of three CO isotopes transferred to the step edge by tip manipulation. The identity of each isotope is indicated. For all spectra, peak positions are displayed as the average of positive and negative bias positions. Error bars are given by the peak fit standard errors in the peak position.

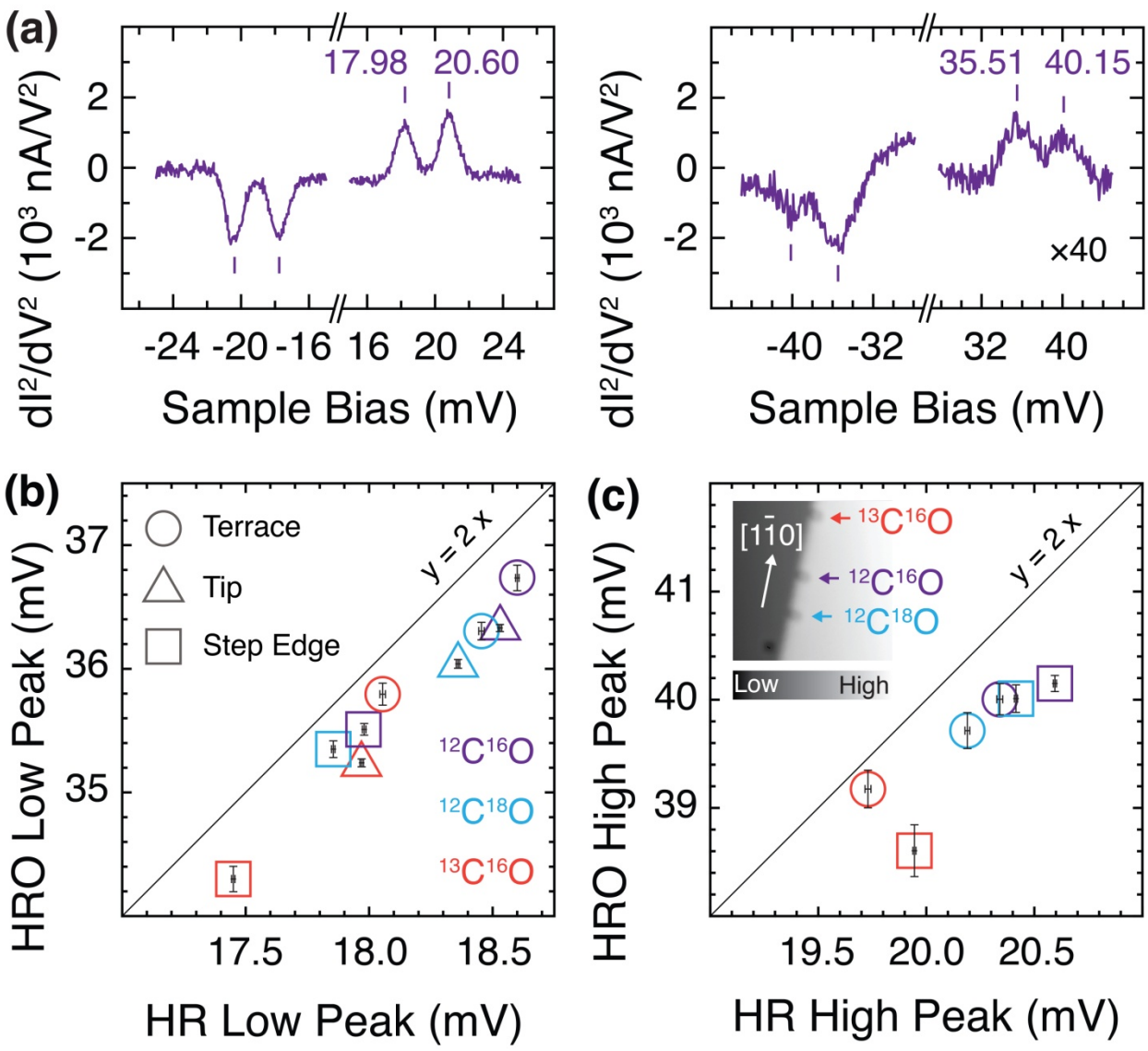
(a)
17.98
20.60
35.51
40.15
×40
dI²/dV² (10³ nA/V²)
Sample Bias (mV)
(b)
Terrace
Tip
Step Edge
y = 2 x
HRO Low Peak (mV)
HR Low Peak (mV)
(c)
[1$\bar{1}$0]
Low
High
HRO High Peak (mV)
HR High Peak (mV)

CHAPTER 3

Conclusions and Future Prospects

3.1 Concluding Remarks

The ability to resolve overtones with STM-IETS has now been convincingly demonstrated, both in this work and in light of other recent studies [1,2]. We have shown here that the anharmonicity of a model adsorbate can be measured with adsorption site specificity, revealing variation among different sites as well as anisotropy in the anharmonicity of a highly asymmetric adsorption site. Since CO is often considered the quintessential model adsorbate on metal surfaces [3] and is a simple, small molecule with well characterized adsorption geometries, the present work presents an ideal experimental baseline for theory to address. The value of the experiment outlined in this work is not exclusively limited to CO molecules of course, and can be generalized to any systems where overtones can be observed. We hope future experiments can make use of STM-IETS measurements of overtones to probe different adsorption environments in which a molecule has been deliberately placed, as demonstrated here for the first time.

What remains then is further theoretical development required to understand why overtones can be observed with CO/Ag(110) and (seemingly) not in most other adsorbate systems studied with STM-IETS so far. Already we have suggested here that destructive quantum interference effects proposed previously for CO [4,5] may be suppressing the elastic tunneling channel, reducing the signal background for the inelastic tunneling channel responsible

for IETS signals as seen in both recent theory [6] and experiment [2] in cross-conjugated molecules.

3.2 Proposed Future Experiments

Preliminary results obtained by our group indicate that the CO hindered rotation overtone is not readily observed with STM-IETS for CO/Cu(001), which suggests that it may not be observable on all surfaces CO is adsorbed onto. Since the excitation energy is ~ 35 meV for CO/Cu(001) compared to ~ 20 meV on CO/Ag(110), it is possible that the (more shallow) adsorption potential well on Ag(110) is also significantly more anharmonic. It is often the case that strongly anharmonic bonds have stronger overtone cross-sections, so this may account for why we could not resolve the overtone for CO/Cu(001), although this does not rule out other unrelated effects of course. If strong anharmonicity is a central requirement, the implication is that CO overtone signals could be made stronger by selecting a surface where the binding energy and/or lateral hopping barrier for CO is expected to be even lower, such as the more inert Ag(001), Ag(111) or Au(111) surfaces. Some caution is advised in employing this strategy however, since if the lateral hopping barrier becomes too low then the CO molecules will simply diffuse when the first overtone is excited, which will allow action spectroscopy measurements but prevent (much more precise) STM-IETS measurements of interest in this work.

Another, more intriguing route to enhancing the overtone cross section may come from selecting a molecule which exhibits Fermi resonances [7–9], which typically occur when the overtone of one vibration is accidentally degenerate in energy with the fundamental of a different vibration. When this occurs, the normally weak overtone signal from the first vibration mode can

become quite strong, seemingly “borrowing” intensity from the fundamental of the second vibration mode, and resulting in a lifting of the degeneracy in the two modes so that a doublet of peaks is observed. It is important to note that the two different vibrations must not only be accidentally degenerate, but share the same symmetry and be localized to the same atoms within the polyatomic molecule. In recent work by Liu et. al., dI/dV measurements of single porphycene molecules adsorbed on Cu(110) appeared to show strong dip/peak features which they assign to overtones of N-H bending modes. These overtone signals are in turn speculated to be enhanced by a Fermi resonance with the nearly degenerate N-H stretch within the porphycene central cavity [1].

Another well-studied adsorbate in surface science, methoxy (methoxide), is the canonical example of Fermi resonance in adsorbed molecules. Methoxy is studied due to its central role as an intermediate in the reaction of methanol with transition metals [10] and it has also served as a simple model system of an adsorbate with a functional group. The Fermi resonances between its symmetric C-H stretch and both symmetric and asymmetric bend modes have presented serious challenges to understanding its spectral features, resulting in controversy in the literature over whether the molecule adsorbs upright or tilted with respect to the surface normal on many surfaces. However it has also played a key role in the eventual proper identification of its adsorption geometry [11].

I would like to propose here that methanol molecules be dosed onto a partially pre-oxidized Cu or Ag surface [10–12] at low temperature, which will react with oxygen atoms to form methoxy if raised briefly to room temperature. The substrate can then be subsequently cooled back down to helium temperatures for STM measurements of methoxy radicals generated from this surface reaction. If successful, STM-IETS could be used to characterize the signal

intensity of both the fundamental modes and Fermi resonances that may be observable and which have been studied in-depth using reflection-absorption infrared spectroscopy on many other metal surfaces [11]. If both the fundamental bending modes and their overtones (in Fermi resonance with the symmetric C-H stretch) could be detected with STM-IETS, they may also be tunable through mechanical or chemical coupling to the local environment of the methoxy molecule. Specifically, the tuning of the Fermi resonance could come from red(blue)shifting the participating stretching and bending modes, which in turn could be achieved by mechanical means by inducing intermolecular vibrational coupling with another methoxy molecule [13], or through chemical means by attaching a hydrogen-bond accepting molecule such as CO to the STM tip and positioning it above the methoxy group. Although C-H groups are typically considered very poor hydrogen bond donors [14], recent Atomic Force Microscopy studies with CO-terminated tips positioned over vertically oriented aromatic rings suggest that it may be possible to measure C=O···H-C chemical forces [15]. Even weak chemical interactions would likely result in significant shifts of the different vibration modes as well as as-yet unknown effects on the IETS cross sections of different vibrational modes. The Fermi resonances can also be tuned by partial isotope substitution with deuterium atoms, which has been exploited in the past to shift the various vibration modes in and out of Fermi resonance [16]. This sort of experiment would allow for unprecedented studies of the Fermi resonance effect in addition to providing a playground of easily observed overtones. Since Fermi resonance is a quantum mechanical state-mixing effect, detailed experimental data is essential as input into quantum chemistry models used to understand otherwise difficult to assign spectral features, such as those in the C-H stretch spectral region [17].

3.3 Bibliography

[1] S. Liu, D. Baugh, K. Motobayashi, X. Zhao, S. V. Levchenko, S. Gawinkowski, J. Waluk, L. Grill, M. Persson, and T. Kumagai, Phys. Chem. Chem. Phys. **20**, 12112 (2018).

[2] C. Salhani, M. L. Della Rocca, C. Bessis, R. Bonnet, C. Barraud, P. Lafarge, A. Chevillot, P. Martin, and J.-C. Lacroix, Phys. Rev. B **95**, 165431 (2017).

[3] G. A. Somorjai, *Introduction to Surface Chemistry and Catalysis* (Wiley, New York, 1994).

[4] J. A. Nieminen, E. Niemi, and K. H. Rieder, Surf. Sci. **552**, L47 (2004).

[5] A. Gustafsson, N. Okabayashi, A. Peronio, F. J. Giessibl, and M. Paulsson, Phys. Rev. B **96**, 085415 (2017).

[6] J. Lykkebo, A. Gagliardi, A. Pecchia, and G. C. Solomon, ACS Nano **7**, 9183 (2013).

[7] E. Fermi, Zeitschrift Für Phys. **71**, 250 (1931).

[8] G. Herzberg, *Molecular Spectra and Molecular Structure. Volume II: Infrared and Raman Spectra of Polyatomic Molecules* (Van Nostrand Reinhold Company, New York, 1945).

[9] D. C. Harris and M. D. Bertolucci, *Symmetry and Spectroscopy: An Introduction to Vibrational and Electronic Spectroscopy* (Dover Publications, New York, 1989).

[10] W. S. Sim, P. Gardner, and D. A. King, J. Phys. Chem. **99**, 16002 (1995).

[11] M. P. Andersson, P. Uvdal, and A. D. MacKerell, J. Phys. Chem. B **106**, 5200 (2002).

[12] Q. Dai and A. J. Gellman, Surf. Sci. **257**, 103 (1991).

[13] Z. Han, G. Czap, C. Xu, C. Chiang, D. Yuan, R. Wu, and W. Ho, Phys. Rev. Lett. **118**, 036801 (2017).

[14] S. J. Knak Jensen, T. H. Tang, and I. G. Csizmadia, J. Phys. Chem. A **107**, 8975 (2003).

[15] S. Kawai, T. Nishiuchi, T. Kodama, P. Spijker, R. Pawlak, T. Meier, J. Tracey, T. Kubo, E. Meyer, and A. S. Foster, Sci. Adv. **3**, 1 (2017).

[16] P. Uvdal, M. K. Weldon, and C. M. Friend, Phys. Rev. B **50**, 12258 (1994).

[17] E. L. Sibert, D. P. Tabor, N. M. Kidwell, J. C. Dean, and T. S. Zwier, J. Phys. Chem. A **118**, 11272 (2014).

APPENDIX A

Additional Experimental Data

A.1 Distribution of CO Isotopes on the Ag(110) Surface

To characterize the distribution of isotopes on the surface, a survey of HR IETS peak positions was conducted for 28 CO molecules, with the results presented as a plot of high HR peak position vs low HR peak position in Fig. A.1. The distribution of peak positions falls into three groups, verifying the presence of three different isotopes on the surface. Some of the variation in the peak positions for each isotope can be attributed to the use of multiple tip terminations used over the course of the 28 measurements as well as lower averaging (4-10 passes averaged) used for efficient data-acquisition.

A.2 Determination of CO binding site on the Step Edge

To determine the binding site of CO molecules deposited from the tip apex to the step edge, another CO molecule can be transferred to the tip and scanned over a CO on the step edge at small tunneling gap in order to achieve atomic resolution of the surface as seen in Fig. A.2(b). CO molecules were found to appear as ellipses with semi-minor axis oriented along the $[1\bar{1}0]$ direction and a protrusion in the center when scanned with a CO tip at feedback setpoint 10 mV/0.5 nA. As this elliptical shape was seen with all CO tip terminations across many tip apex conditions and experiments, we believe this is caused by anisotropic relaxation of the CO on the terrace toward the CO on the tip as the tip is approached laterally toward the terrace CO. In all

cases we found that CO takes the Ag(110) atop site on the terrace as well as the terminating step edge.

A.3 Additional STM-IETS Measurements

STM-IETS measurements of the HT mode for all three CO isotopes attached to the tip as well as HR and HR overtone modes for CO adsorbed on the step edge for the $^{13}C^{16}O$ and $^{12}C^{18}O$ isotopes were omitted from the main text for brevity but are included here for completeness. These spectra are shown in Fig. A.3.

Figure A.1: Hindered Rotation Peak Positions for 28 CO Molecules. The peak positions are plotted as points on a graph of high doublet peak position vs low doublet peak position, so that each point corresponds to two peaks (high and low). Errors in the peak fits are displayed as semi-transparent rectangular boxes centered on each point. d^2I/dV^2 measurements were performed with either 600 μV_{RMS} or 1 mV_{RMS} bias modulation. The isotopes fall into three groups, with the assignment shown in the figure obtained from the high resolution spectra shown in the main text.

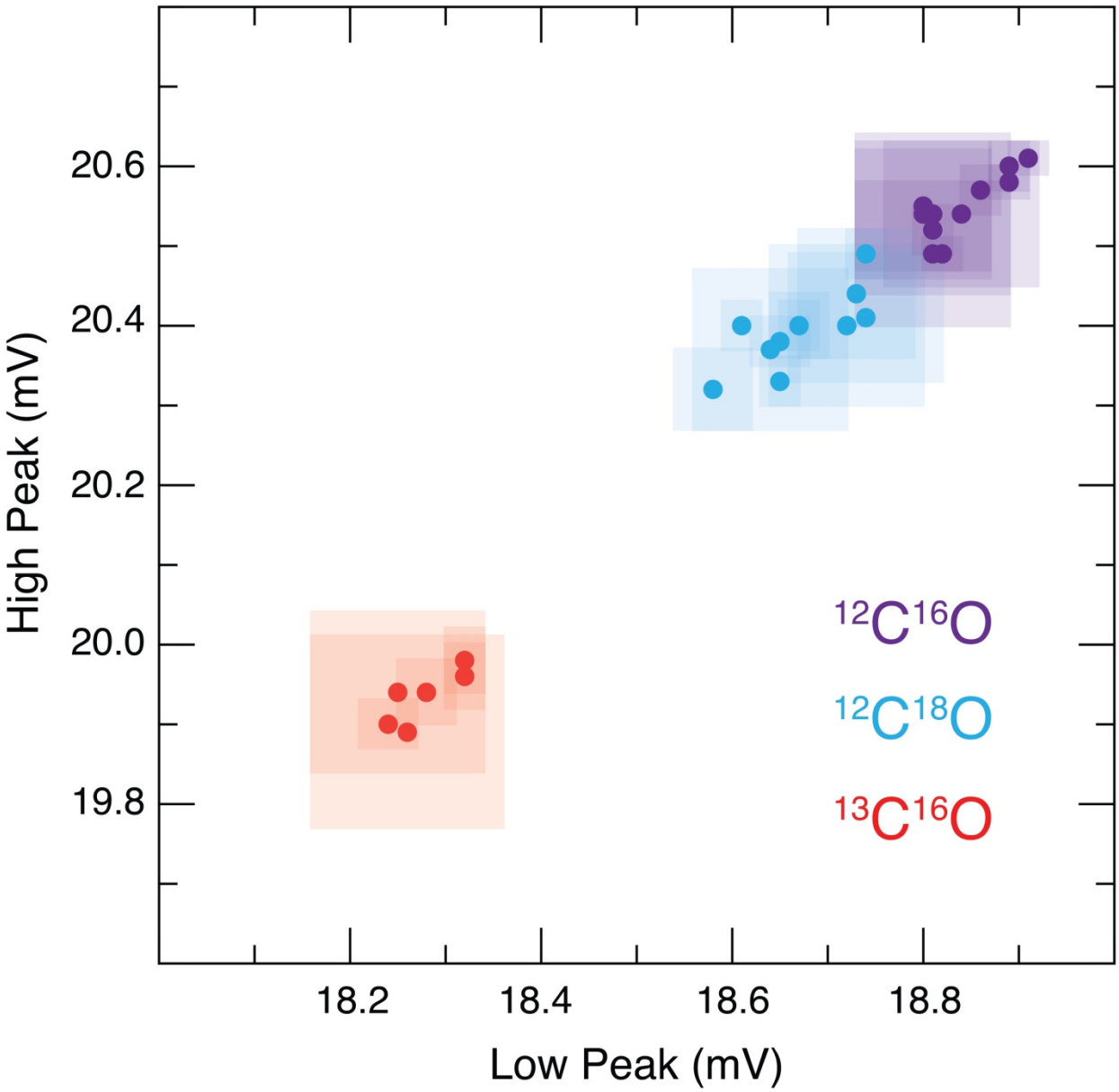
20.6
20.4
20.2
20.0
19.8
High Peak (mV)
18.2
18.4
18.6
18.8
Low Peak (mV)
12C16O
12C18O
13C16O

Figure A.2: Determination of CO Adsorption Site on the $[1\bar{1}0]$ Step Edge. (a) Constant current STM topography with bare metal tip acquired with tunneling setpoint 10 mV/0.3 nA and image size 80 × 80 Å. (b) Constant current STM topography with CO-terminated tip acquired with tunneling setpoint 10 mV/0.5 nA and image size 64 × 64 Å. The Ag(110) lattice mesh is overlaid for clarity. The bright object at the bottom right is a single Ag atom deposited onto the surface from controlled contact between the tip and substrate.

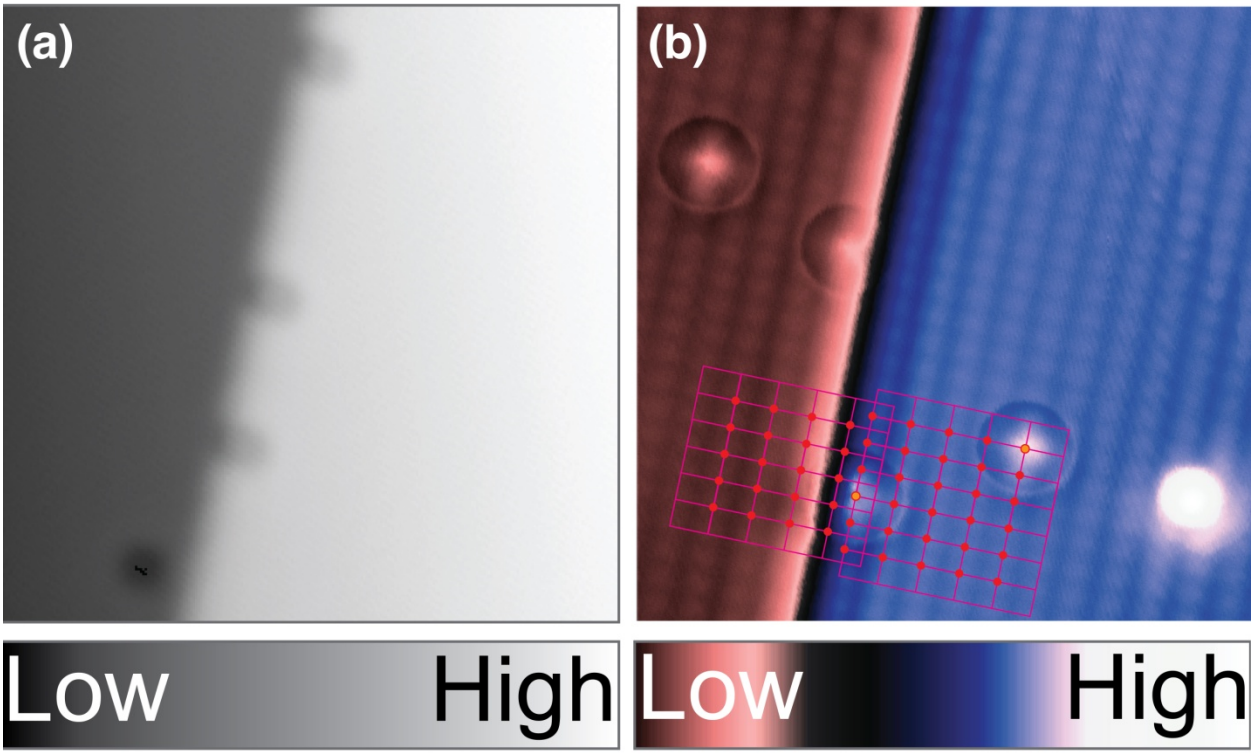
(a)
(b)
Low
High
Low
High

Figure A.3: Additional STM-IETS Measurements. (a) HT spectra for all three isotopes adsorbed onto the STM tip. Note that this metal tip apex termination differed from the tip used for the HR and HR overtone spectra in Fig. 3(c) in the main text. (b) HT spectra for all three isotopes adsorbed onto the $[1\bar{1}0]$ step edge. All HT spectra were taken with 300 μV_{RMS} bias modulation at 311.11 Hz. (c) HR spectra for all three isotopes adsorbed on the step edge, taken with 600 μV_{RMS} bias modulation at 311.11 Hz. (d) HR overtone spectra of all three isotopes adsorbed on the step edge, taken with 2 mV_{RMS} bias modulation at 471 Hz.

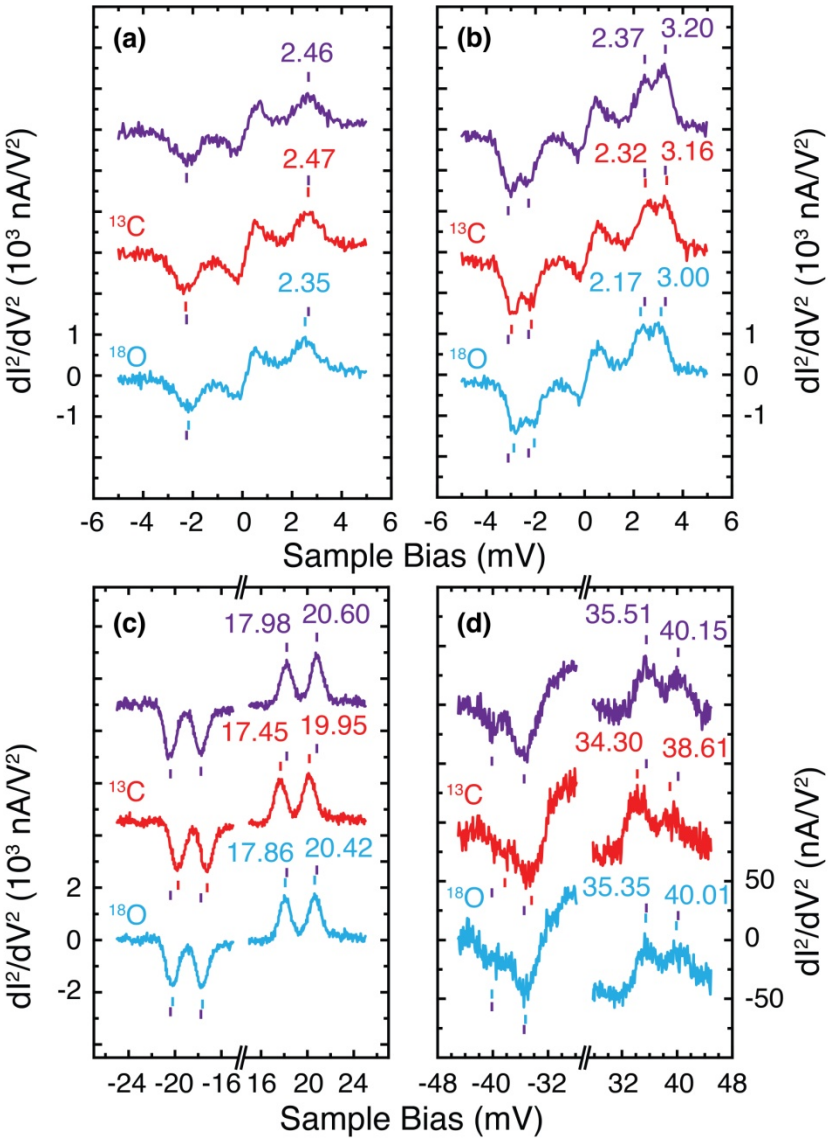
(a)
2.46
2.47
13C
2.35
18O
(b)
2.37
3.20
2.32
3.16
13C
2.17
3.00
18O
dI²/dV² (10³ nA/V²)
Sample Bias (mV)
(c)
17.98
20.60
17.45
19.95
13C
17.86
20.42
18O
(d)
35.51
40.15
34.30
38.61
13C
35.35
40.01
18O
dI²/dV² (nA/V²)

APPENDIX B

Determination of the Anharmonicity Constants and Errors

B.1 Determination of the Anharmonicity Constant χ_e

The potential energy surface for bending modes (HT and HR) can be expected to be more symmetric about the equilibrium position on the terrace and tip geometries than for the modes normal to the surface (M-CO and CO stretch), which should follow a more traditional Morse-like shape. Nevertheless one can still approximate the anharmonicity using the traditional higher-order correction to the quantum harmonic oscillator energy eigenvalues which are derived from solving the Schrodinger equation using a Morse potential instead of a harmonic potential [1]:

$$E(n) = \hbar\omega\left(n + \frac{1}{2}\right) - \chi_e\hbar\omega\left(n + \frac{1}{2}\right)^2$$

Where χ_e is the anharmonicity constant.

A vibrational excitation $v = 0 \rightarrow v = 2$ would have experimentally-measured activation energy of:

$$\Delta E_{HRO} = E(2) - E(0) = 2\hbar\omega - 6\chi_e\hbar\omega,$$

while vibrational excitation $v = 0 \rightarrow v = 1$ would yield:

$$\Delta E_{HR} = E(1) - E(0) = \hbar\omega - 2\chi_e\,\hbar\omega$$

With experimentally measured values for ΔE_{HRO} and ΔE_{HR}, one obtains the relations for $\hbar\omega$ and χ_e as

$$\hbar\omega = 3\Delta E_{HR} - \Delta E_{HRO}, \qquad \chi_e = \frac{2\Delta E_{HR} - \Delta E_{HRO}}{6\Delta E_{HR} - 2\Delta E_{HRO}}$$

The anharmonicity constants displayed in Table S1 were obtained in this way. Note the similarity to the anharmonicity constants for the HR mode in this work to the value 0.0156 ± 0.0051 found for the Ag-CO stretch obtained from the lateral hopping experiment in [2].

B.2 Determination of Percent Anharmonicity and Errors

Throughout this work, standard errors in fitted peak center position are used. The peak positions reported in the main text are the average of positive and negative bias, which are assumed to be uncorrelated measurements with uncorrelated peak fits. The errors in the positive/negative bias peak fits were then assumed to obey the standard Propagation of Error formula [3]

$$\Delta E_{avg} = \frac{1}{2}(\Delta E_{+} + \Delta E_{-})$$

$$s_{avg} = \sqrt{\left(\frac{\partial \Delta E_{avg}}{\partial \Delta E_{+}}\right)^2 {s_{+}}^2 + \left(\frac{\partial \Delta E_{avg}}{\partial \Delta E_{-}}\right)^2 {s_{-}}^2} = \frac{1}{2}\sqrt{{s_{+}}^2 + {s_{-}}^2} \ ,$$

where s_{+} and s_{-} are the standard deviations of the fitted peak position for positive and negative bias, respectively.

For the percent anharmonicity, errors are computed as

$$P_{Anh} = 100\frac{2\Delta E_{HR} - \Delta E_{HRO}}{2\Delta E_{HR}}$$

$$s_{P_{Anh}} = \sqrt{\left(\frac{\partial P_{Anh}}{\partial \Delta E_{HR}}\right)^2 {s_{HR}}^2 + \left(\frac{\partial P_{Anh}}{\partial \Delta E_{HRO}}\right)^2 {s_{HRO}}^2} = 50\sqrt{\frac{{\Delta E_{HRO}}^2 {s_{HR}}^2 + {\Delta E_{HR}}^2 {s_{HRO}}^2}{{\Delta E_{HR}}^4}}$$

For the anharmonicity constant χ_e, the errors are computed as

$$\chi_e = \frac{2\Delta E_{HR} - \Delta E_{HRO}}{6\Delta E_{HR} - 2\Delta E_{HRO}}$$

$$s_{X_e} = \sqrt{\left(\frac{\partial \chi_e}{\partial \Delta E_{HR}}\right)^2 {s_{HR}}^2 + \left(\frac{\partial \chi_e}{\partial \Delta E_{HRO}}\right)^2 {s_{HRO}}^2} = \frac{1}{2}\sqrt{\frac{{\Delta E_{HRO}}^2 {s_{HR}}^2 + {\Delta E_{HR}}^2 {s_{HRO}}^2}{(\Delta E_{HRO} - 3\Delta E_{HR})^4}}$$

Finally, for $\hbar\omega$ the errors are computed as

$$\hbar\omega = 3\Delta E_{HR} - \Delta E_{HRO}$$

$$s_{\hbar\omega} = \sqrt{\left(\frac{\partial \hbar\omega}{\partial \Delta E_{HR}}\right)^2 {s_{HR}}^2 + \left(\frac{\partial \hbar\omega}{\partial \Delta E_{HRO}}\right)^2 {s_{HRO}}^2} = \sqrt{9{s_{HR}}^2 + {s_{HRO}}^2}$$

B.3 Bibliography

[1] R. S. Berry, S. A. Rice, and J. Ross, *Physical Chemistry*, Second Ed. (Oxford University Press, Oxford, 2000).

[2] J. Oh, H. Lim, R. Arafune, J. Jung, M. Kawai, and Y. Kim, Phys. Rev. Lett. **116**, 56101 (2016).

[3] P. R. Bevington and D. K. Robinson, *DATA REDUCTION AND ERROR ANALYSIS FOR THE PHYSICAL SCIENCES*, Third Ed. (McGraw-Hill, New York, 2003).

Table B.1: Fitted Peak Positions, Errors and Anharmonicity for CO on Terrace

Terrace

Hindered Translation			Hindered Rotation		
Isotope	Peak Position (mV)	Avg. Peak Position (mV)	Isotope	Peak Position (mV)	Avg. Peak Position (mV)
$^{12}C^{16}O$	-2.15 ± 0.05	2.29 ± 0.03	$^{12}C^{16}O$	-18.40 ± 0.01	18.60 ± 0.01
	2.43 ± 0.04			18.80 ± 0.01	
	-2.93 ± 0.06	3.09 ± 0.04		-20.16 ± 0.02	20.34 ± 0.01
	3.24 ± 0.04			20.52 ± 0.02	
$^{13}C^{16}O$	-2.08 ± 0.04	2.25 ± 0.03	$^{13}C^{16}O$	-17.87 ± 0.02	18.06 ± 0.01
	2.41 ± 0.05			18.24 ± 0.01	
	-2.87 ± 0.05	3.04 ± 0.04		-19.58 ± 0.02	19.73 ± 0.01
	3.20 ± 0.06			19.88 ± 0.02	
$^{12}C^{18}O$	-2.03 ± 0.07	2.15 ± 0.05	$^{12}C^{18}O$	-18.26 ± 0.02	18.46 ± 0.01
	2.27 ± 0.07			18.65 ± 0.01	
	-2.71 ± 0.05	2.91 ± 0.04		-20.02 ± 0.02	20.19 ± 0.01
	3.11 ± 0.06			20.36 ± 0.01	

Table B.1: Fitted Peak Positions, Errors and Anharmonicity CO on Terrace *(Continued)*

Terrace					
Hindered Rotation Overtone					
Isotope	Peak Position (mV)	Avg. Peak Position (mV)	Percent Anharmonicity	χ_e	$\hbar\omega$
$^{12}C^{16}O$	-36.75 ± 0.19	36.74 ± 0.10	1.24 ± 0.27	0.0121 ± 0.0026	19.06 ± 0.11
	36.72 ± 0.08				
	-39.94 ± 0.27	40.01 ± 0.14	1.65 ± 0.35	0.0159 ± 0.0033	21.01 ± 0.15
	40.07 ± 0.10				
$^{13}C^{16}O$	-35.77 ± 0.14	35.80 ± 0.09	0.86 ± 0.26	0.0087 ± 0.0025	18.38 ± 0.09
	35.82 ± 0.11				
	-39.40 ± 0.22	39.18 ± 0.17	0.71 ± 0.43	0.0070 ± 0.0042	20.01 ± 0.18
	38.95 ± 0.27				
$^{12}C^{18}O$	-36.25 ± 0.11	36.31 ± 0.07	1.65 ± 0.20	0.0160 ± 0.0018	19.07 ± 0.15
	36.36 ± 0.09				
	-39.51 ± 0.28	39.72 ± 0.17	1.63 ± 0.42	0.0158 ± 0.0040	20.85 ± 0.17
	39.92 ± 0.18				

Table B.2: Fitted Peak Positions, Errors and Anharmonicity for CO on Tip

Tip					
Hindered Translation			Hindered Rotation		
Isotope	Peak Position (mV)	Avg. Peak Position (mV)	Isotope	Peak Position (mV)	Avg. Peak Position (mV)
$^{12}C^{16}O$	-2.25 ± 0.03	2.46 ± 0.02	$^{12}C^{16}O$	-18.48 ± 0.01	18.53 ± 0.01
	2.66 ± 0.03			18.58 ± 0.01	
$^{13}C^{16}O$	-2.29 ± 0.03	2.47 ± 0.02	$^{13}C^{16}O$	-17.92 ± 0.01	17.97 ± 0.01
	2.65 ± 0.03			18.02 ± 0.01	
$^{12}C^{18}O$	-2.17 ± 0.03	2.35 ± 0.02	$^{12}C^{18}O$	-18.33 ± 0.01	18.36 ± 0.01
	2.52 ± 0.02			18.39 ± 0.01	

Hindered Rotation Overtone					
Isotope	Peak Position (mV)	Avg. Peak Position (mV)	Percent Anharmonicity	χ_e	$\hbar\omega$
$^{12}C^{16}O$	-36.38 ± 0.04	36.33 ± 0.03	1.97 ± 0.10	0.0190 ± 0.0009	19.26 ± 0.04
	36.28 ± 0.04				
$^{13}C^{16}O$	-35.26 ± 0.04	35.24 ± 0.03	1.95 ± 0.10	0.0187 ± 0.0009	18.67 ± 0.04
	35.22 ± 0.05				
$^{12}C^{18}O$	-35.96 ± 0.05	36.04 ± 0.04	1.85 ± 0.12	0.0179 ± 0.0011	19.04 ± 0.05
	36.12 ± 0.05				

Table B.3: Fitted Peak Positions, Errors and Anharmonicity for CO on Step Edge

Step Edge					
Hindered Translation			Hindered Rotation		
Isotope	Peak Position (mV)	Avg. Peak Position (mV)	Isotope	Peak Position (mV)	Avg. Peak Position (mV)
$^{12}C^{16}O$	-2.28 ± 0.07	2.37 ± 0.05	$^{12}C^{16}O$	-17.75 ± 0.01	17.98 ± 0.01
	2.45 ± 0.06			18.21 ± 0.01	
	-3.11 ± 0.05	3.20 ± 0.03		-20.38 ± 0.01	20.60 ± 0.01
	3.29 ± 0.04			20.81 ± 0.01	
$^{13}C^{16}O$	-2.17 ± 0.05	2.32 ± 0.04	$^{13}C^{16}O$	-17.22 ± 0.01	17.45 ± 0.01
	2.47 ± 0.07			17.68 ± 0.01	
	-2.98 ± 0.04	3.16 ± 0.04		-19.73 ± 0.01	19.95 ± 0.01
	3.34 ± 0.07			20.16 ± 0.01	
$^{12}C^{18}O$	-2.05 ± 0.08	2.17 ± 0.06	$^{12}C^{18}O$	-17.63 ± 0.01	17.86 ± 0.01
	2.28 ± 0.09			18.08 ± 0.01	
	-2.88 ± 0.07	3.00 ± 0.05		-20.20 ± 0.01	20.42 ± 0.01
	3.11 ± 0.08			20.63 ± 0.01	

Table B.3: Fitted Peak Positions, Errors and Anharmonicity for CO on Step Edge *(Continued)*

Step Edge					
Hindered Rotation Overtone					
Isotope	Peak Position (mV)	Avg. Peak Position (mV)	Percent Anharmonicity	χ_e	$\hbar\omega$
$^{12}C^{16}O$	-35.47 ± 0.05	35.51 ± 0.05	1.25	0.0122 ± 0.0014	18.43 ± 0.06
	35.55 ± 0.08				
	-40.13 ± 0.10	40.15 ± 0.07	2.55	0.0242 ± 0.0016	21.65 ± 0.08
	40.17 ± 0.11				
$^{13}C^{16}O$	-34.39 ± 0.18	34.30 ± 0.10	1.72	0.0166 ± 0.0027	18.05 ± 0.10
	34.21 ± 0.10				
	-38.27 ± 0.44	38.61 ± 0.24	3.23	0.0304 ± 0.0053	21.24 ± 0.24
	38.94 ± 0.19				
$^{12}C^{18}O$	-35.26 ± 0.09	35.35 ± 0.07	1.04	0.0101 ± 0.0020	18.23 ± 0.08
	35.44 ± 0.10				
	-40.14 ± 0.20	40.01 ± 0.13	2.03	0.0195 ± 0.0030	21.25 ± 0.13
	39.88 ± 0.16				